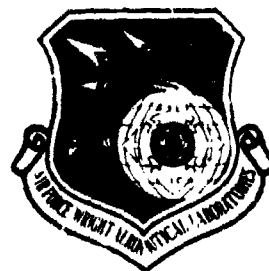AFWAL-TR-80-4081
Part I

AD A094349

INVESTIGATION OF EMAT BASE SYSTEM FOR THE DETECTION OF
BOLT HOLE TYPE CRACKS   Part I - Detection of Cracks in the
Inaccessible Lower Half of Wing Lap Joints Using EMATS

C. V. Vasile
R. H. Houston
R. B. Thompson

Rockwell International Corporation
Science Center
1049 Camino Dos Rios
Thousand Oaks, California 91360

July 1980

TECHNICAL REPCRT AFWAL-TR-80-4081, Part I

Interim Report for Period 31 August 1978 (Task III)

Interim rept.
1 Apr-31 Aug 78,

REPORT DOCUMENTATION PAGE	READ INSTRUCTIONS BEFORE COMPLETING FORM

1. REPORT NUMBER AFWAL-TR-80-4081, Part I	2. GOVT ACCESSION NO. AD A074349	3. RECIPIENT'S CATALOG NUMBER

4. TITLE (and Subtitle)
INVESTIGATION OF EMAT BASE SYSTEM FOR THE DETECTION OF BOLT HOLE TYPE CRACKS - Part I - Detection of Cracks in the Inaccessible Lower Half of Wing Lap Joints Using EMATS

5. TYPE OF REPORT & PERIOD COVERED
Interim Report (Task III)
04/01/78 through 08/31/78

6. PERFORMING ORG. REPORT NUMBER
SC595.44C5A

7. AUTHOR(s)
C. V. Vasile
R. H. Houston
R. B. Thompson

8. CONTRACT OR GRANT NUMBER(s)
F33615-74-C-5180
DARPA Order - 2828

9. PERFORMING ORGANIZATION NAME AND ADDRESS
Rockwell International Corporation
Science Center
1049 Camino Dos Rios
Thousand Oaks, California 91360

10. PROGRAM ELEMENT, PROJECT, TASK AREA & WORK UNIT NUMBERS
7351

11. CONTROLLING OFFICE NAME AND ADDRESS
Materials Laboratory
Air Force Wright Aeronautical Laboratories
Air Force Systems Command
Wright-Patterson Air Force Base, Ohio 45433

12. REPORT DATE
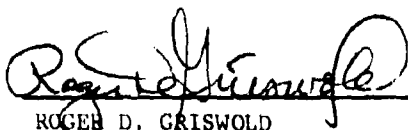July 1980

13. NUMBER OF PAGES
67

14. MONITORING AGENCY NAME & ADDRESS(if different from Controlling Office)

66

15. SECURITY CLASS. (of this report)
Unclassified

15a. DECLASSIFICATION, DOWNGRADING SCHEDULE

16. DISTRIBUTION STATEMENT (of this Report)

Approved for public release; distribution unlimited.

17. DISTRIBUTION STATEMENT (of the abstract entered in Block 20, if different from Report)

18. SUPPLEMENTARY NOTES

19. KEY WORDS (Continue on reverse side if necessary and identify by block number)

Electromagnetic-acoustic transducers; EMAT; cracks under fasteners; ultrasonic testing; wing lap joints; quantitative flaw detection; nondestructive evaluation; nondestructive testing

20. ABSTRACT (Continue on reverse side if necessary and identify by block number)

The detection of saw slots in an aircraft wing lap joint is demonstrated with EMATS (electromagnetic acoustic transducers) utilizing 250 KHz horizontal shear acoustic waves reflected from the fastener area. A real-time Fourier transform signal processor was developed and used to gather experimental data and generate plots of power vs. frequency as well as the complex transform. A simple ultrasonics model is described which is capable of explaining many of the features of the experimental data.

DD FORM 1473 1 JAN 73   EDITION OF 1 NOV 65 IS OBSOLETE

FOREWORD

This report describes an in-house effort conducted by personnel of the Rockwell International Science Center, under Project 7351 (DARPA order 2828) of General Order 595, "Interdisciplinary Program for Quantitative Flaw Definition."

The work reported herein was performed during the period 1 April 1978 to 31 August 1978, under the direction of the author, Dr. C. V. Vasile. The report was released by the author in November 1978.

This report is Part I of two parts concerned with detection of cracks under fasteners with EMATS (electromagnetic acoustic transducers).
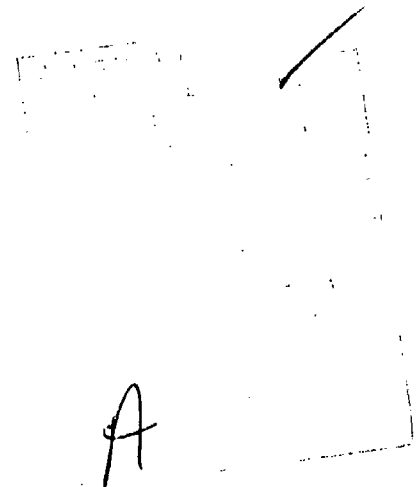
TABLE OF CONTENTS

LIST OF ILLUSTRATIONS

LIST OF ILLUSTRATIONS (continued)

I. INTRODUCTION AND SUMMARY

This report describes a five-month study having as an objective the demonstration of feasibility and generation of design data for an ultrasonic technique for the nondestructive evaluation (NDE) of fastener holes in the lower, inaccessible section of an aircraft wing lap joint. The resulting measurement technique utilizes the excitation of horizontally polarized shear (SH) waves at 250 KHz (0.5 in. (1.27 cm) wavelength in aluminum) with non-contact, periodic permanent magnet electromagnetic transducers (EMATs) and a dedicated electronics test set. The transducers are placed on the accessible portion of the wing adjacent to the fastener hole in question and the flaw information is separated from signals introduced by geometrical complexities of the structure by real time, Fourier analysis techniques.

More specifically a pair of EMATs are placed <u>as close as possible</u> to a single fastener hole, thereby forming an "ultrasonic filter" structure. The presence of the hole perturbs the passband of this filter, while the presence of a crack introduces a further significant change in both the amplitude and phase response of the "filter." In order to make this observation it is necessary to perform a real-time Fourier analysis of the ultrasonic signals. Accomplishing this task required considerable effort in modifying and improving the performance of an existing correlation receiver and dedicated test set. While such effort detracted from the amount of test data we would otherwise have collected, development of this improved electronic signal processing was essential in gathering meaningful and reproducible data.

In summary, we have: (1) developed a real-time Fourier transform signal processor, (2) used it to gather experimental data demonstrating the feasibility of detecting cracks growing from fasteners in lap joints of fixed geometry, and (3) deduced a simple ultrasonics model capable of explaining many of the experimental data. The primary problem which remains is the fact that changes in the geometry of the wing lap joint produce interfering

1

effects, and further work must be done to learn to generate reliable crack information in regions where such changes are occurring or the geometry is unknown. Based on these results, we recommend a second phase, the goal of which would be to design and construct an improved test inspection system, use it to gather a more extensive baseline data set on a statistically meaningful number of samples, and analyze the data to develop specific approaches for obtaining flaw information in regions of geometrical changes and to verify the reliability of the resulting algorithms.

II. BACKGROUND

The problem is summarized in Fig. 1. The upper half of a lap joint can be inspected by available techniques, such as the Rotoscanner. However, the lower half is not as easily inspected. This has been attributed to variations in the ultrasonic transmission properties of the thin sealant layer (a matter that is discussed further in the Appendix). Our approach combines four innovative ideas. Noncontact EMATs are used to excite horizontally polarized shear waves on member B. These propagate around the corner and enter the lap joint region. There they are scattered by the hole, crack combination, and this information propagates back around the corner to a receiving transducer, also on member B. Finally, the flaw information is deduced from the other geometrical information by signal processing, in this case near real time Fourier analysis using a correlation receiver. The remainder of this section provides background data which illustrates these ideas, as they existed at the time of initiation of the program.

Fig. 2 illustrates the basic principles of an EMAT (electromagnetic-acoustic transducer), a device which can excite ultrasonic waves with no couplant, through a loosely bonded paint layer. In its most elementary form, it consists of a single wire, next to a metal part, which excites eddy currents at the desired ultrasonic frequency. If a static magnetic field is also provided, these eddy currents will experience Lorentz forces (the same forces which drive an electric motor), and ultrasonic waves are radiated. These waves can be detected by reciprocal processes.

A real transducer is composed of an array of wires and magnets which produce the forces required to form the desired beam. One such configuration, known as the PPM (periodic permanent magnet) is shown in the right half of Fig. 2. This excites horizontally polarized shear (SH) waves which are polarized parallel to the metal surface. Such waves are particularly useful for the present problem because they do not mode convert upon reflection from

3

THE PROBLEM:
TO DETECT CRACKS IN LOWER PLATE OF WING LAP JOINT

CRACKS IN UPPER PLATE DETECTABLE BY
EXISTING TECHNIQUES

FUEL TANK
SEALANT

CRACKS IN LOWER
PLATE NOT DETECTABLE
BY CONVENTIONAL
TECHNIQUES BECAUSE
OF HEAVY ATTENUATION   WING LAP JOINT
AND REFLECTION OF
SEALANT.

A

B

APPROACH:

● EMATS

● MODES AROUND CORNERS

● SCATTERING

● DEDICATED SIGNAL PROCESSING
  HARDWARE USED TO INTERPRET
  SIGNALS BY FOURIER ANALYSIS

Fig. 1 Detection of Cracks under Fasteners.

4

P. P. M.

PERIODIC MAGNET EMAT

ELECTRICAL COIL

SAMARIUM COBALT MAGNETS

FORCES

$$\vec{F} = \vec{J} \times \vec{B}$$

SH WAVE

SINGLE WIRE

J_ω

I_ω

H_ω

M_0

M_ω

H_0

FORCE ON LATTICE: LORENTZ FORCE

MAGNETOSTRICTION
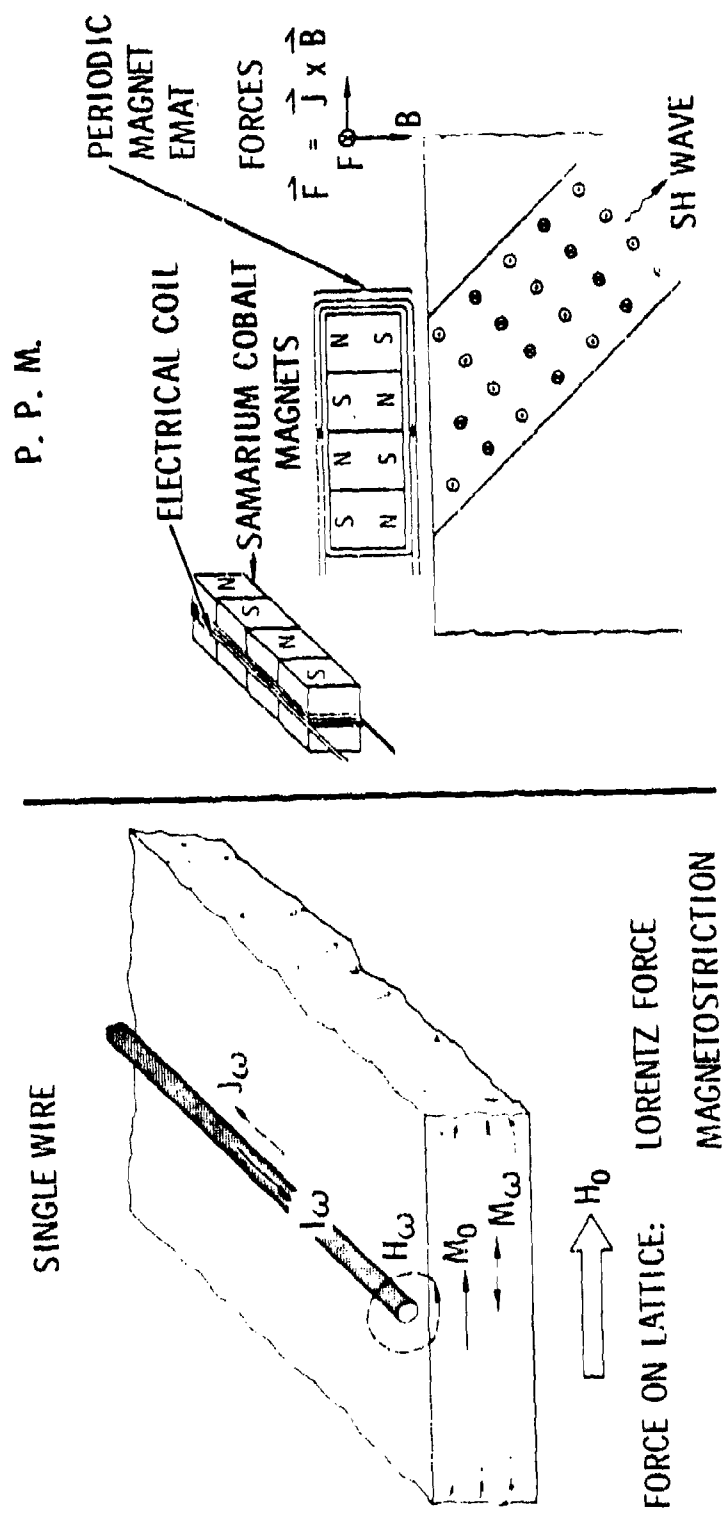
Fig. 2 Couplant Free Inspection with EMATs.

5

parallel surfaces. They can only be excited by EMATs, since fluid coupled angle beam systems do not support this component of shear. In this program, the transducer structure has evolved to one further level of sophistication, as shown in Fig. 3. Here the magnets have been separated into two oppositely polarized stacks, and the coil is in the form of a hairpin loop. Since both the magnetic bias and current change direction, the force is the same as in the previous configuration. However, the electrical properties of the structure are greatly improved.

Fig. 4 illustrates the principles of guided wave propagation which are being used. There are a number of ultrasonic modes which can propagate along a flat plate. These are characterized by a particular profile of displacement and stress (lower right) and whose frequency ($f = \omega/2\pi$) and wavelength (λ) are related by a set of dispersion curves (lower left). These modes can propagate around corners, with some reflection, and thereby sense flaws in the lap joint region.

Fig. 5 presents a set of experiments which were performed to demonstrate the ability to detect cracks growing from holes by measuring the scattering properties of these waves. For these measurements, the nondispersive, $n = 0$, mode was selected. The upper two sets of data show the scattering measured for a 1/4 in. (0.635 cm) hole in the center of a 1/8 in. (0.318 cm) plate, as measured at 500 KHz. To the left we see the scattering properties of the hole. To the right we see the changes produced when an 0.3 in. (0.768 cm) saw slot was placed in the hole. The bottom two sets of data show the results that were obtained when the hole was near the edge, rather than in the center, of the plate. The extra reflection from the edge complicates the signals, but again the cracked hole is clearly distinguishable.

In order to separate the flaw information from that due to other geometrical effects, signal processing is required. Fig. 6 illustrates

6

New

Previous
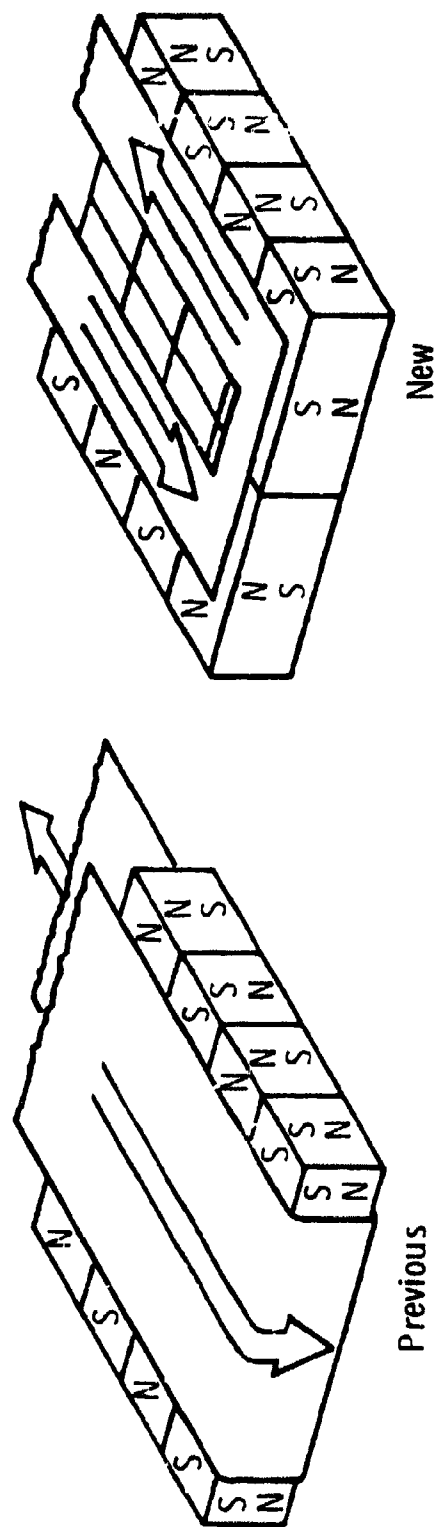
Fig. 3 EMAT Configurations.

7

- THIN SKIN ACTS AS A WAVEGUIDE WHICH CHANNELS ENERGY TO LOWER JOINT

  B

  ENERGY TO FLAW

  ENERGY RETURNS ONLY AFTER LARGE TIME DELAY
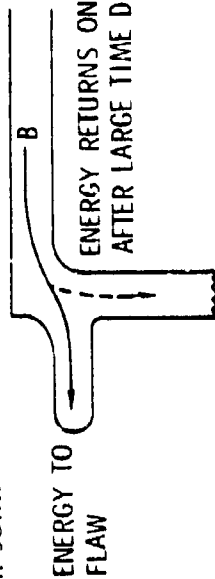
- DISPERSION CURVE SHOULD BE USED TO SELECT FREQUENCY AND WAVELENGTH

$y = +b/2$ FREE BOUNDARY $V_x(y)$ $T_{xy}(y)$ $T_{xy}(y)$

$y = b/2$ FREE BOUNDARY

n = 1 MODE

$y = +b/2$ FREE BOUNDARY $U_x(y)$ $T_{xy} = 0$ $T_{xz}(y)$

$y = b/2$ FREE BOUNDARY

n = 0 MODE

$\omega b/V_s$

n = 5, 4, 3, 2, 1, n = 0

$\frac{3}{\beta} = V_s$

IMAGINARY βb REAL βb

$V_s = (c_{44}/\rho)^{1/2}$

—— SYMMETRIC
- - - ANTISYMMETRIC

Fig. 4 Waveguide Effects.

8

CONFIGURATION

HOLE WITH
SIMULATED CRACK

PLATE EDGE

INCIDENT WAVE

SCATTERED WAVE

0.3 IN. CRACK

INCIDENT WAVE

MEASURED ULTRASONIC AMPLITUDES FOR
HOLE IN CENTER OF PLATE
(NO EDGE EFFECTS)

INCIDENT WAVE

NO CRACK

MEASURED ULTRASONIC AMPLITUDES FOR
HOLE NEAR EDGE OF PLATE

INCIDENT WAVE

0.3 IN. CRACK

INCIDENT WAVE

NO CRACK

INCIDENT WAVE

Fig. 5 Scattering from Cracked Hole.

9

VOLTAGE .25" HOLE

.3" L SLOT

IN-PHASE (I) AND OUT-OF-PHASE (Q)
COMPONENTS VERSUS ANGLE

AMPLITUDE

NO SLOT

BACKSCATTERING VERSUS ANGLE
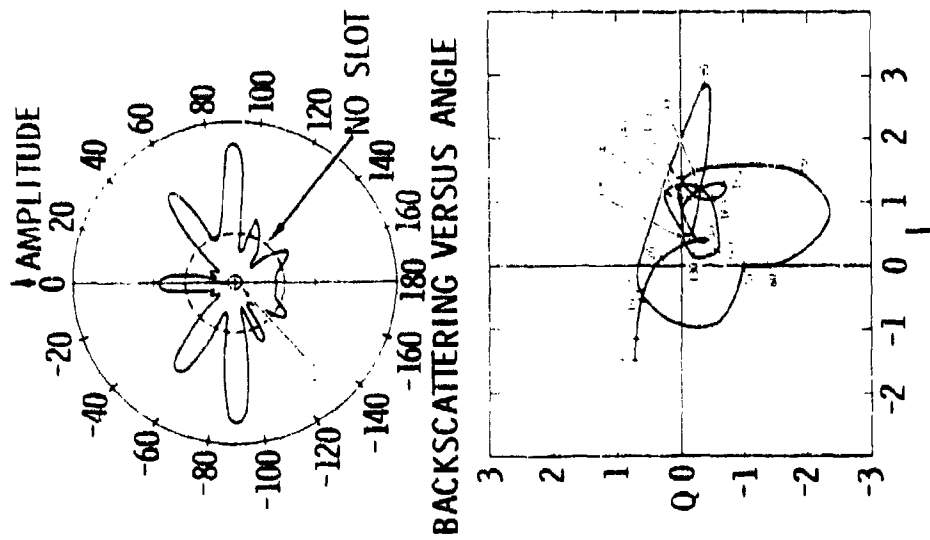
I PLOTTED VERSUS Q
WITH FREQUENCY AS A PARAMETERS
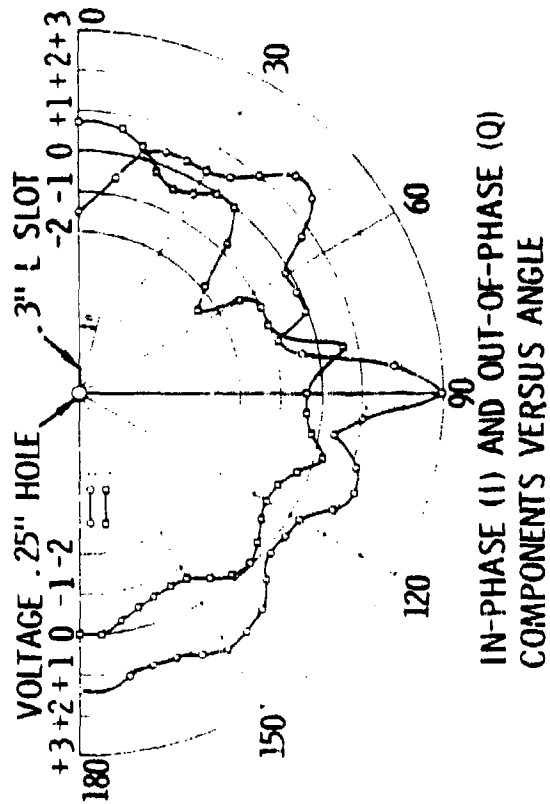
Fig. 6 Signal Processing.

10

several candidate procedures. In the upper left is shown a plot of the magnitude of the backscattered signal from a slotted hole. The phase information, suppressed in that presentation, is revealed in the display to the right. Here,both the in-phase (I) and out-of-phase (Q) components of the signal are shown as a function of angle. These may be thought of as the sine and cosine transforms of the signal. A possibly more useful representation of this information is presented at the bottom left. Here the I component is plotted versus the Q component with angular orientation as a parameter. The resulting display is quite similar to that which has proved so powerful in the presentation and interpretation of eddy current data.

The remainder of the report describes how these elements, EMATs, SH modes propagating around corners, scattering, and signal processing, have been combined to develop a candidate solution to the problem.

III. SYSTEM CONCEPT

Fig. 7 illustrates a representative cross section of the structure to be inspected. The troublesome area is the lower lip of the joint as it cannot be accessed from below in practice. The approach we selected was to locate a transmitting EMAT on member B and direct ultrasonic energy in the form of the lowest order, horizontally polarized plate mode (e.g., the $n = 0$ SH mode) past the fastener and measure the phase and amplitude characteristics of the transmitted signal as detected by a similar receiving EMAT.

The dimensions illustrated in Fig. 7 are merely representative of actual structures and were used in the fabrication of a mock-up measuring 24 x 24 in. (61 x 61 cm) containing 19 D size drill holes (.246 in. (0.62 cm) dia) spaced 1-1/4 in. (3.18 cm) on centers. Actual wing sections have tapered fastener holes, nonuniform hole spacings as well as nonuniform dimensions and sealant in the joint. Therefore, it is important to design a test system that can minimize and/or account for these variable geometrical parameters in order to avoid obscuring the presence of a crack which is the geometrical discontinuity which we are seeking.

Fig. 8 illustrates the location of a pair of EMATs and some important path lengths in the configuration that was ultimately selected. Note the symmetrical location of transmitter and receiver and the fact that a narrow wing section can be used since the back radiation patterns of the EMATs are not directed towards each other, even in the presence of a back reflecting edge. This is important for practical reasons. As illustrated, identical EMATs (with the exception of different matching transformers) are used for transmitter and receiver. The three ultrasonic wave paths indicated in Fig. 2 are drawn from the center of phase of each four-period long transducer and are key in the simple model to be described below.

12

NOTE MATERIAL - 7075 A1

1¼" BETWEEN BOLTS

½" BOLT, 3/8" LEAD* (See below)

SEALANT

9/32"

3 5/16"

3/16"

1 1/8"

1/4"

B

C

1 7/16"

7/32"

1/2"

1 5/32"

D

7/16"

11/16"

A

TYPICAL FASTENER DIMENSIONS

.094"
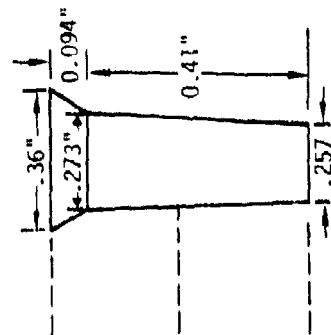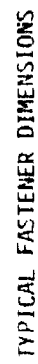
.36"

.273"

0.41"

.257

13

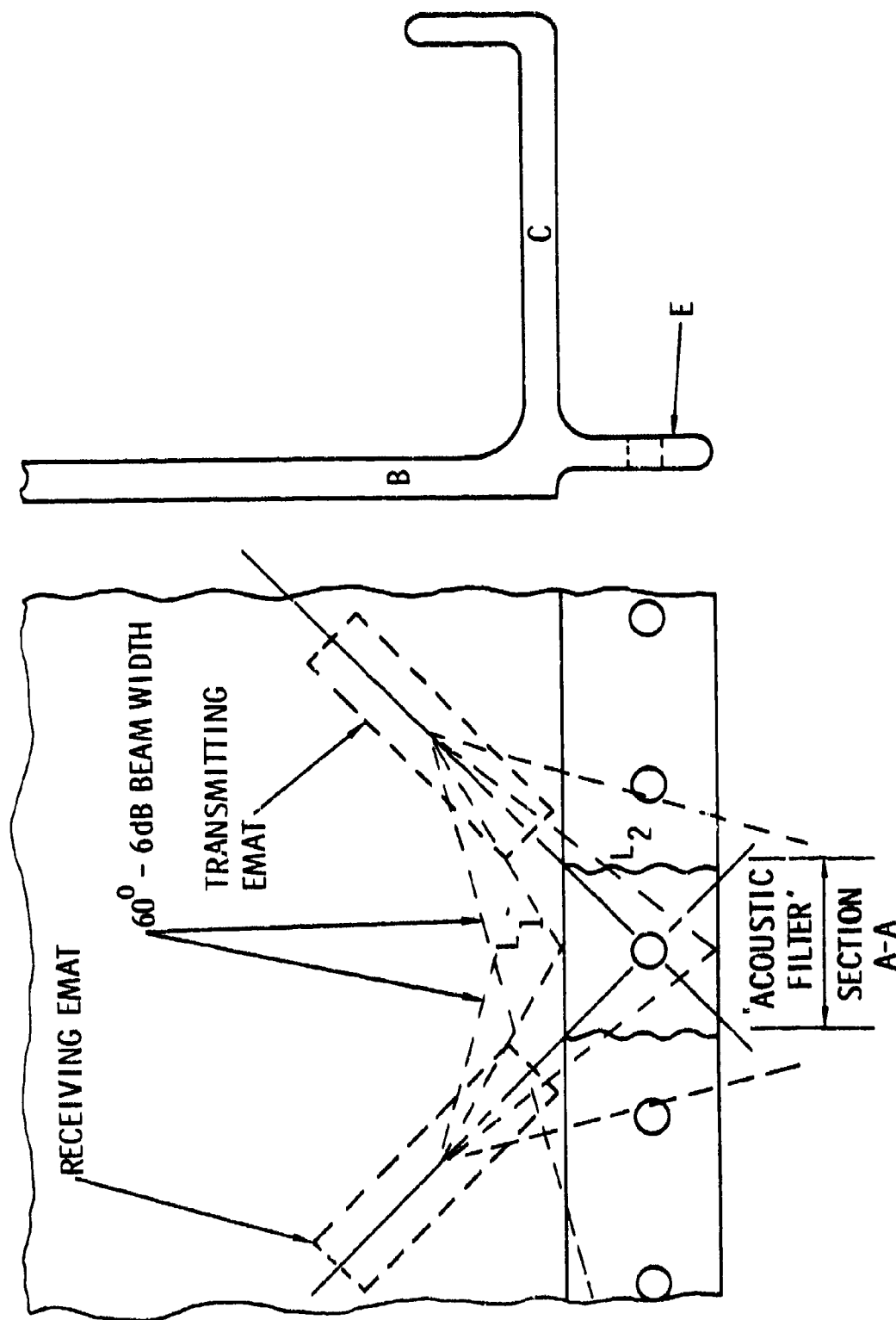Fig. 7 Representative Cross-Section of Wing Lap Joint.

Fig. 8 Location of SH Wave EMATs with Respect to Fastener Hole.

14

The transducer configuration was arrived at after numerous theoretical and experimental investigations. Early in the program we used transducers having a .25 in. (0.64 cm) period which therefore operated on a 9/32 in. (0.71 cm) thick aluminum plate at .488, .54, .645, .78, .92, and 1.1 MHz for the n = 0, 1, 2, 3, 4, 5 SH modes, respectively. Early in the program a large wing section mock-up was not available and a broadband system was therefore set up in order to make measurements on flat plates, right angle bends, and jogs with all of these modes.

The driving force behind higher frequency and therefore higher mode operation was the feeling that high frequency operation was desirable because better collimated beams could be achieved, thereby reducing the effects of adjacent holes in the resulting scattered fields. However, a number of disadvantages readily became apparent: (1) the operating frequency and excitation efficiency are a strong function of plate thickness (member B in Fig. 1) for the higher order modes (n > 0); (2) the presence of bends and jogs affects the higher order modes differently; and finally, but most importantly, (3) the actual structure was found to exhibit waveguiding properties wherein energy became trapped in the lower lap, and propagated along the joint scattering energy from many holes. This made it impossible to eliminate the effects of adjacent holes with the frequency limitations imposed by practical EMATs. This waveguiding effect was established with the mock-up which became available near the end of the program and actually proved the original transducer configuration to be unfeasible.

Thus, a different approach became necessary and the original far-field scattering ideas were discarded. First, we assembled a set of transducers having an 0.5 in. (1.27 cm) period which could be operated in the n = 0, SH mode at 244 kHz, thereby making the operating frequency independent of plate thickness and the excitation efficiency variation a weaker function of transducer liftoff and plate thickness. Second, we located the transducer, as illustrated in Fig. 8, as close as was feasible to the hole in question,

thereby performing scattering measurements in the near field. Third, we limited the transmitter pulse duration to a 2-5-cycle tone burst and gated the received signal to reject, as best we could, the direct feedthrough signal as well as signals scattered from adjacent holes and the end of member C (Fig. 8). Fourth, we implemented a measurement system, illustrated schematically in Fig. 9, and described in detail in section V. Fifth, we viewed the section A-A, indicated in Fig. 8, as an acoustic bandpass filter structure having a predictable, and reproducible, phase and amplitude response. Thus, by taking this new viewpoint, the inspection scheme becomes one of displaying the complex Fourier transform of the received, time-gated signals which is the product of frequency response of a linear system composed of the structure, EMAT and electronics. The presence of a crack modifies the passband shape of the structure and thus produces a change in the Fourier transform. We are thus effectively measuring a crack induced change in the mechanical response of the joint.

A second set of more recent experiments on actual wing sections in which the fasteners and sealant were present have suggested an alternate, albiet more complicated, measurement scheme illustrated in Fig. 10. Here three transducers are placed on top of the wing, with two on one side of the front and a third on the other side so that the transmission properties of the $n = 0$ SH, mode through the joint can be taken advantage of. Before the real wing sections became available we reasoned that the low acoustic impedance of the sealant would cause the two parts of the lap joint to be essentially uncoupled, acoustically so that this transmission would not occur. This is, in fact, true for the case of ultrasonic waves normally incident upon a joint at frequencies of several MHz as would be the case if a piezoelectric transducer were placed upon the top surface of the wing joint and an attempt were made to make a high frequency inspection of the lower half (see Appendix A). However, for the $n = 0$, SH waveguide mode propagating along the wing, the effect of the sealant is negligible at low frequencies, as discussed in Appendix A. Thus, for the geometry of Fig. 10, an $n = 0$, SH wave will

16

Fig. 9 Measurement System Block Diagram.

17

EMAT

0.5 IN. PERIOD
4 PERIODS

XMTR

RCVR

BOTTOM LAP SECTION

END OF TOP LAP

90°

1-18/64 IN.

1-18/64 IN.

SEALANT

END OF BOTTOM LAP

1-18/64 IN.

TOP LAP SECTION

RCVR
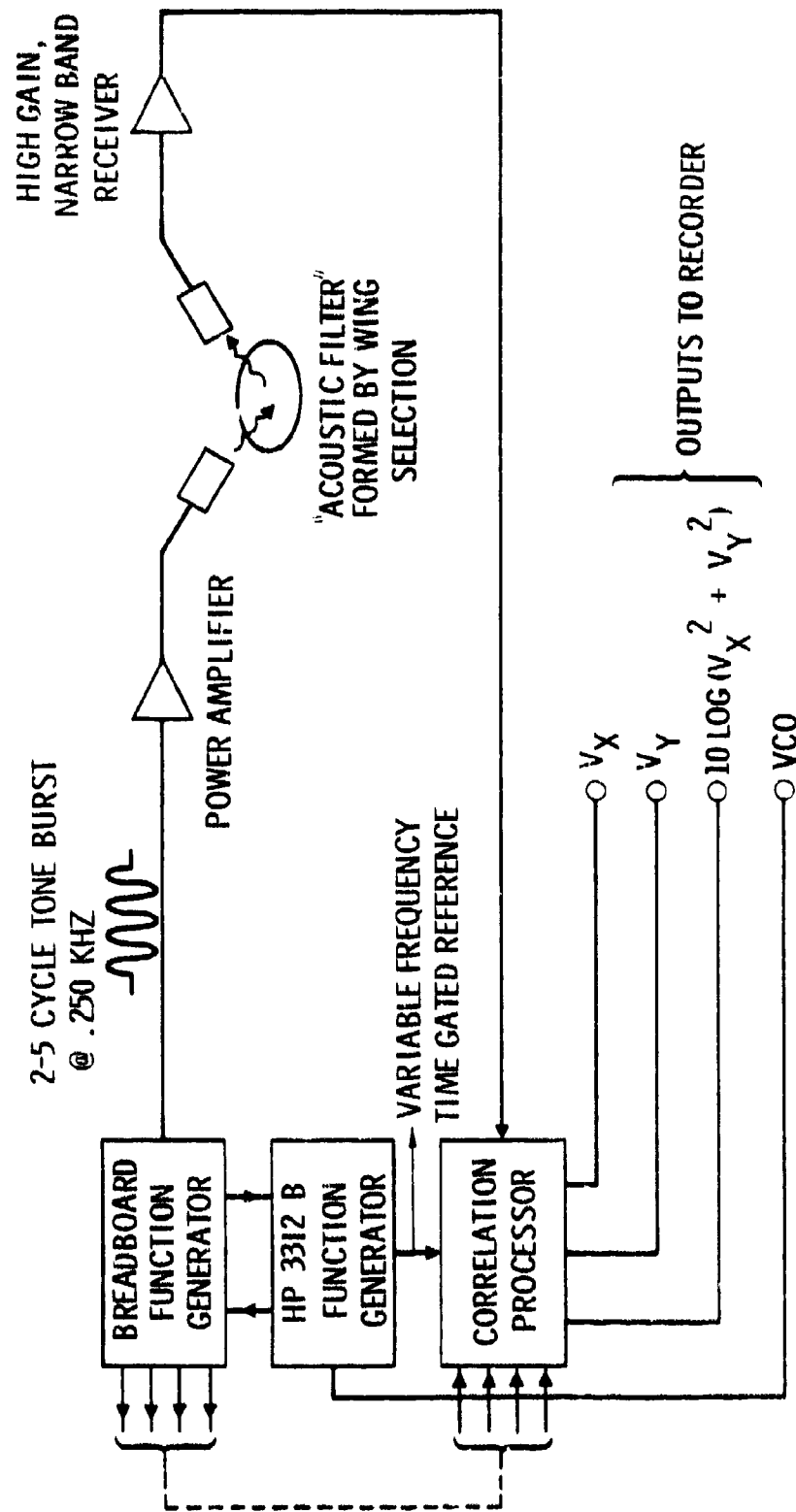
Fig. 10 Transmission Configuration.

18

travel across the joint quite efficiently. This was a completely unexpected result, hence little experimental data is available. The significance of the Fig. 10 configuration is that independent information is obtained which may complement that of the previous configuration to help discriminate against effects due to geometrical changes.

IV. THEORETICAL ANALYSIS OF SYSTEM

The configuration shown in Fig. 8 was selected on the basis of measurements of ultrasonic scattering. Fig. 11 compares the measured SH wave radiation pattern for a four-period long, n = 0 EMAT and that produced when the beam strikes an 0.25 in. (0.635 cm) dia. hole. The data was obtained on a large flat plate having a thickness t = 0.25 in. (0.635 cm), by locating the transmitter the same distance from the hole as in Fig. 8 and rotating the receiver about the hole while keeping it aimed at the hole. For comparison, we have illustrated the wing section member E of Fig. 8 by dashed lines at the location that it would occupy in the proposed inspection configuration.

It should be noted that, had we rotated the transducer about the center of the transmitter, a somewhat narrower beam pattern would have been measured in which the -3 db width was 46° and the -6 db width was 60°.

The key results deduced from these radiation pattern and scattering measurements are: (1) energy is confined about a single hole in the inspection scheme illustrated in Fig. 8 and (2) on forward transmission the hole modifies the radiation pattern of the transducer, but considerable energy (only .9 db forward loss) passes by the hole to reflect from the edge of member E in Fig. 8, and (3) little energy is scattered at 90°. Thus, when the transducers are positioned as shown, the hole can be expected to have minimal influence on the ultrasonic signals. Based upon these radiation pattern measurements, we can derive a simple model of the ultrasonic reflection process in the absence of sealant and fasteners; i.e., only the part of the lap joint shown in Fig. 8.

Fig. 12(a) is a schematic representation of the entire signal transmission process. A two-cycle, 244 kHz, tone burst is input to a four-period EMAT, thereby exciting an n = 0,SH wave having an 0.5 in. (1.27 cm) long wavelength. The SH wave is filtered by the wing section geometry of

20

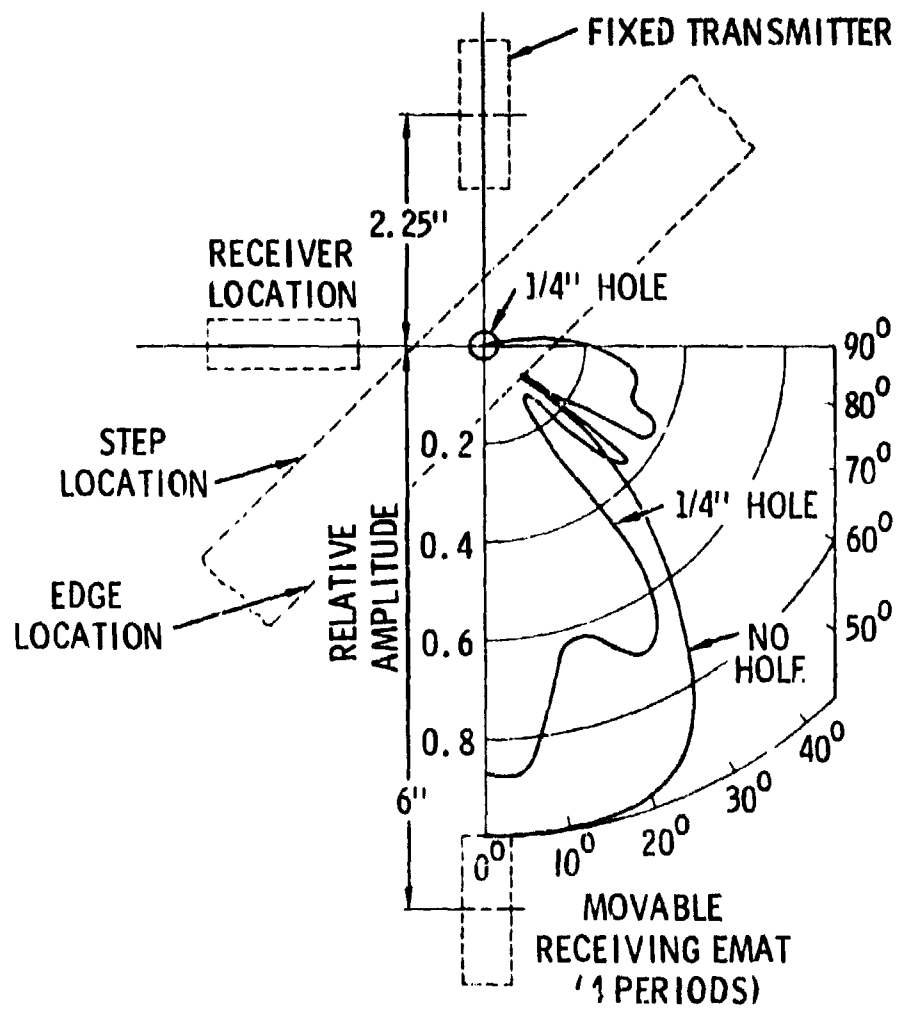Fig. 11 SH-Radiation Patterns for the n = 0 Mode at 0.22 kHz ($\lambda = 0.5$).

(a) SCHEMATIC REPRESENTATION OF SIGNAL TRANSMISSION PROCESS

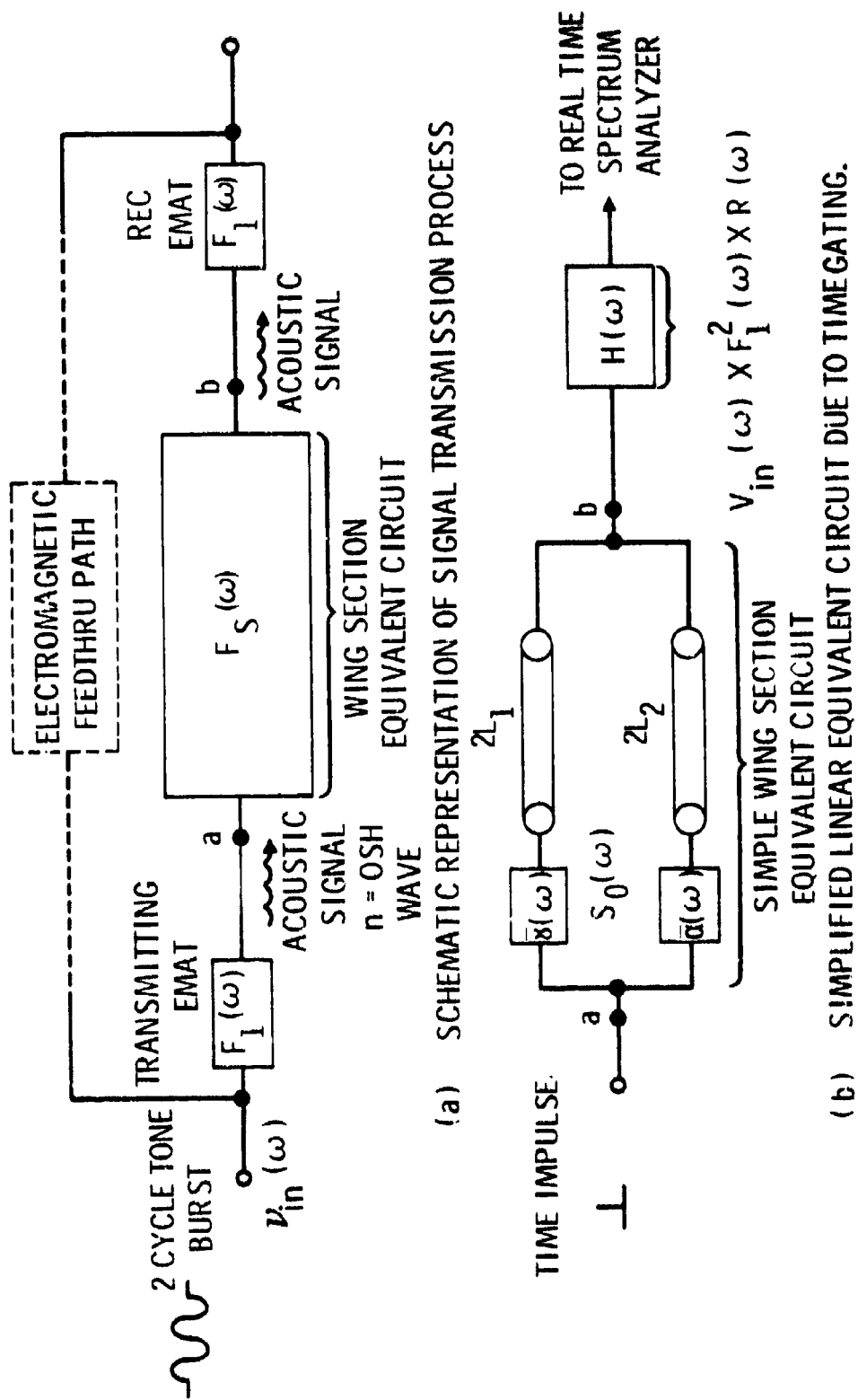(b) SIMPLIFIED LINEAR EQUIVALENT CIRCUIT DUE TO TIMEGATING.

Fig. 12 Equivalent Circuit Model of Wing Section.

Fig. 8 and subsequently received by an identical receiving EMAT, amplified and filtered. As indicated in Fig. 12(a), each element in the chain has a frequency response.

The objective is to measure the effect a crack has on the wing section transfer function $F_s(\omega)$, and thereby deduce the length of the crack. The simplified equivalent circuit of Fig. 12(b) is arrived at as follows. $H(\omega)$ denotes an equivalent system impulse response which is determined by calculation or by measuring the direct transmission of an SH wave between two transducers on a large 9/32 in. (0.71 cm) plate. Time gating is used to eliminate the effects of electromagnetic feedthrough and other interferring signals such as reflections from sample edges. In addition to the EMAT response, $F_1(\omega)$, the spectral characteristics of the driving voltage, $V_{in}(\omega)$, and of the receiving amplifier, $R(\omega)$, are included.

The actual wing section transfer function $F_s(\omega)$ is extremely difficult to calculate since it is due to a very complicated and analytically intractable structure. However, if we restrict the frequency band of interest by designing $H(\omega)$ appropriately, then based on the scattering data discussed above as well as experimental observation a first order approximation is to replace $F_s(\omega)$ by $S_0(\omega)$ as in Fig. 12(b). Here we assume that energy can propagate from transmitter to receiver by either of the two paths shown in Fig. 8. Path 1 is due to a reflection off the step of Fig. 8, characterized by an amplitude transfer function $\bar{\gamma}(\omega)$ and a delay path $2L_1$. The second signal path has a length $2L_2$ and an amplitude response is characterized by $\bar{\alpha}(\omega)$. This corresponds to energy entering the joint and reflecting from its edge. $\bar{\alpha}(\omega)$ is what we are seeking because it is affected by the presence and shape of the fastener hole.

The reason there is not a third delay path corresponding to the hole location is due to the fact that little energy is scattered at 90° from a hole as was illustrated in Fig. 11.

23

An actual wing section will exhibit variations in the thickness of members B and C, Fig. 8, which affects both $H(\omega)$ and $S_0(\omega)$, as well as variations in the length of member C which affects L_2 and $\bar{a}(\omega)$. Furthermore, the presence of the sealant will cause energy to be coupled to the second member. Even so there will still be two main signal paths, L_1 and L_2, due to the discontinuities indicated in Fig. 12. There will be additional information about the possibility of flaws in the upper half of the joint because energy is coupled through the sealant into this region as well.

To effectively deal with these structural variations, a calibration procedure must be arrived at. With the aid of Fig. 12(b) we see that L_1 is set by the transducer placement and is, therefore, known. L_2 will be known from the wing design and $\bar{\gamma}(\omega)$ will change in a simple and controlled way because the step height does not change that much. The success of the inspection process will hinge upon associating changes in the transmitted signal with changes in $\bar{a}(\omega)$, independent of these known varations.

In order to develop a model, we will calculate $H(\omega)$ and $S_0(\omega)$ independently. Vasile and Thompson[1,2] give expressions for SH wave excitation in metal plates. For present purposes, it is possible to simplify and adapt these results in order to exhibit some important features that have been observed experimentally. Thus, by assuming zero skin depth, neglecting transducer end effects and diffraction, and noting that the forward transfer impedance is proportional to ω/β_n (β_n = SH plate mode propagation constant) we can derive an expression for the frequency dependence of $H(\omega)$:

$$H(\omega) = H_0 \cdot R(\omega) \cdot T(\omega) \cdot \left| Z_0(\omega) + Z_1(\omega) + \text{etc.} \right| \tag{1}$$

where H_0 is an arbitrary scale factor, $R(\omega)$ is the electronic receiver frequency response, $T(\omega)$ is the Fourier transform of the input current waveform given approximately by:

$$T(\omega) \simeq \text{sinc} \left[\pi(f-f_0) N_c/f_0 \right] \tag{2}$$

24

$\omega = 2\pi f$, sinc $x = \sin x/x$, N_c = number of carrier cycles, f_0 = carrier frequency and the bracketed terms give the transducer response denoted $F_1{}^2(\omega)$ in Fig. 12. This analysis differs slightly from that shown in Fig. 12(b) since we are specifying the input current, $T(\omega)$, rather than voltage $V_{in}(\omega)$.

The bracketed terms in Eq. (1) are expressed as a sum of normalized forward transfer impedances of the plate modes which are dependent upon the EMAT parameters, plate material and thickness. For present purposes we consider the first two modes and have:

$$Z_0(\omega) \approx \left(\frac{\pi}{2}\right)^2 \text{sinc}^2\left[\frac{\pi(f-f_0)N}{f_0}\right] \text{sinc}^2\left[\frac{\pi}{2}\frac{f}{f_0}\right] e^{-i\frac{2\pi f}{V_s}L_D} \tag{3}$$

$$Z_1(\omega) \approx \left(\frac{\pi}{2}\right)^2 \frac{2}{\left[1-\left(\frac{f_{c1}}{f}\right)^2\right]^{1/2}} \text{sinc}^2\left[\frac{\pi N}{f_0}\left(\sqrt{f^2 - f_{c1}{}^2} - f_0\right)\right] \times$$

$$\text{sinc}\left(\frac{\pi}{2}\frac{f}{f_0}\right)\sqrt{1-\left(\frac{f_{c1}}{f}\right)^2} \quad e^{-i\frac{2\pi f}{V_s}L_D\sqrt{1-\left(\frac{f_{c1}}{f}\right)^2}} \tag{4}$$

Similar terms would be obtained for $Z_n(\omega)$, $n > 1$. Here: V_s = shear wave velocity (3111 m/s), L_D is the length of the transmission path, $f_0 = (V_s \div$ transducer period), $f_{c1} = (nV_s/2t)_{n=1} = 218$ kHz = cutoff frequency of $n = 1$ mode for the $t = 9/32$ in. plate thickness, $t = 9/32$ in., and N = number of periods in the transducers = 4.

The reason for including only the first two modes is demonstrated by the dispersion relation shown in Fig. 13. The long dashed line corresponds to a set of 0.5 in. (1.27 cm) period EMATs operating on a 9/32 in. (0.71 cm)
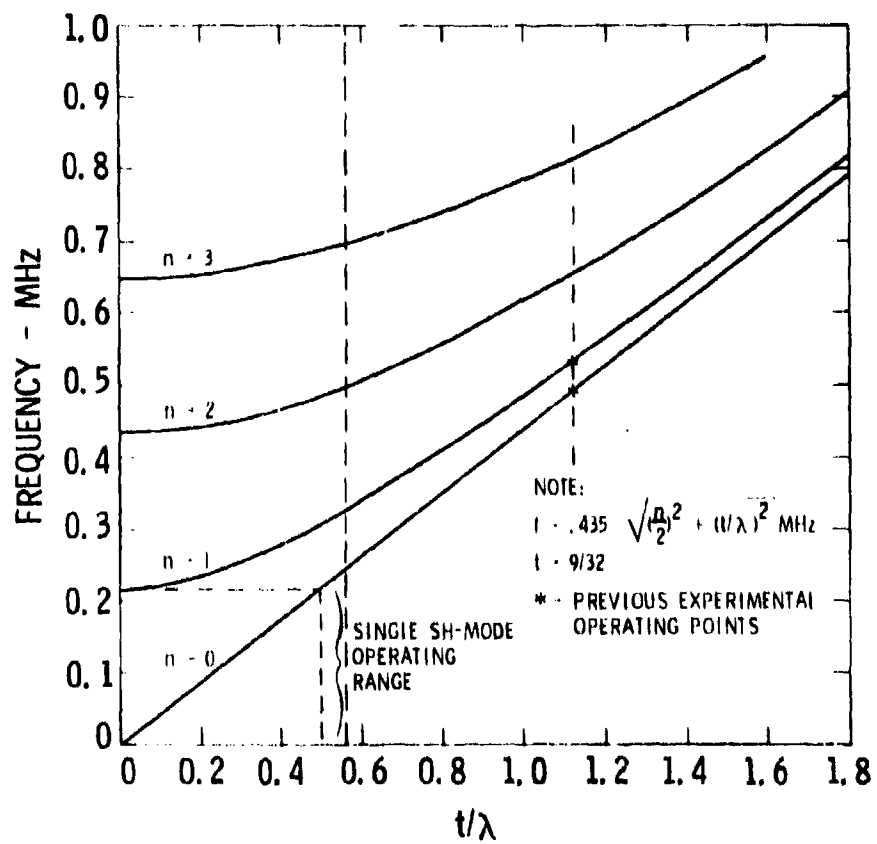
Fig. 13 SH-Dispersion Relation for a 9/32" Aluminum Plate.

plate. At any point where the dashed line crosses a solid line, a single mode can be excited by a monochromatic drive. For a tone burst, several modes can be excited with amplitudes determined by the spectral content of the burst. For our case, the $n = 0$ and $n = 1$ modes are important.

The transducers ultimately used were not originally designed for this project and became available late in the program from other work. Hence they were not fully optimized for this particular problem. Because of time resolution problems associated with electromagnetic feedthrough suppression and geometrical reflections, we limited the lengths of the EMATs to four periods (2 in. (5 cm) long) and limited the 250 kHz drive current burst to two or three cycles, even though eight cycles would have provided maximum signal levels as well as better higher order mode suppression. The consequence of these limitations are illustrated in Fig. 14, which contains individual sketches of $R(\omega)$, $T(\omega)$, $Z_0(\omega)$, and $Z_1(\omega)$ for $f_c = 250$, $N = 4$, and $N_c = 2$ in. (5 cm). Also shown are sketches of the combination appearing in Eq. (1) which seem to give $H(\omega)$. From the lower plot it is clear that the $n = 1$ mode will contribute significantly in a direct transmission measurement and this has been observed experimentally. Thus a better system design requires lower frequency operation and longer period transducers so that the $n = 1$ mode is cutoff and $Z_1(\omega) \ll Z_0(\omega)$ over the band of interest.

Fortunately, for the geometry of Fig. 8 where the acoustic transmission path involves a complicated reflection/scattering process, it appears that the contribution of $Z_1(\omega)$ is reduced because: (1) the 7/32 in. (0.56 cm) thick member E is cutoff to the $n = 1$ mode at frequencies below 280 kHz so that it does not contribute to path 2 and (2) the incident $n = 1$ mode appears to incur a higher loss upon reflection off the step so that its effect is lower in path 1 than it is in direct transmission. Thus, based upon these observations, it is reasonable to neglect the $n = 1$ mode in developing a first order model of the wing structure for the $n = 0$ mode as was done in drawing the equivalent circuit in Fig. 12(b).
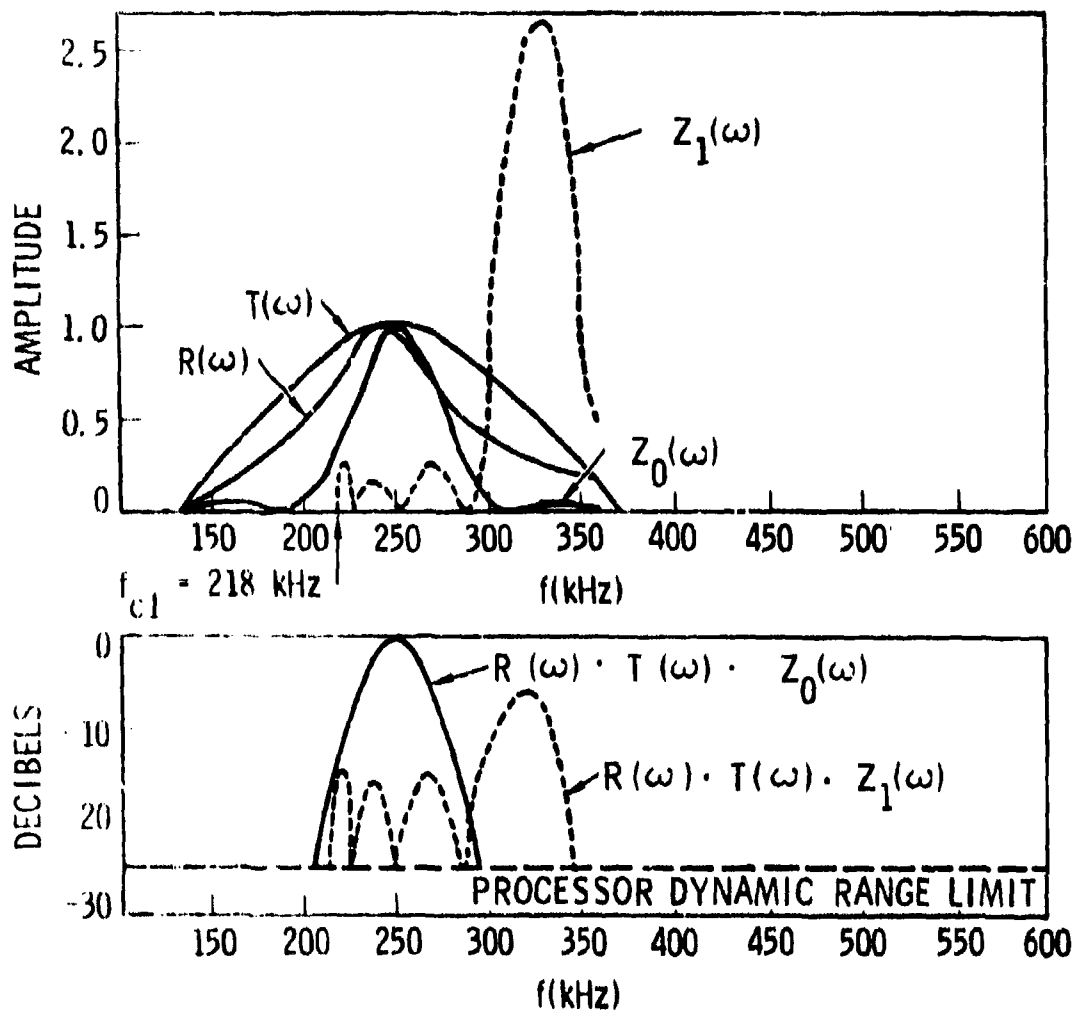
27

Fig. 14 Components for H (ω) for Direct Transmission.

28

From the single mode equivalent circuit of Fig. 12(b) we compute the structure transfer function $S_0(\omega)$ which, when multiplied by an appropriate transfer function $H(\omega)$, gives the overall system/transfer function $S_0(\omega) \times H(\omega)$ which we measure. The result is:

$$S_0(\omega) = \overline{\gamma}(\omega)\, e^{-i\,\frac{2\omega L_1}{V_s}} + \overline{\alpha}(\omega)\, e^{-i\,\frac{2\omega L_2}{V_s}} \tag{5}$$

or

$$S_0(\omega) = \overline{\gamma}(\omega)\, e^{-i\,\frac{2\omega L_1}{V_s}} \left[1 + \frac{\overline{\alpha}(\omega)}{\overline{\gamma}(\omega)}\, e^{-i\,\frac{2\omega}{V_s}(L_2 - L_1)} \right] \tag{6}$$

From measurements on the geometry of the wing mock-up illustrated in Fig. 8: $L_1 = 1.85$ in. (4.7 cm); $2L_1/V_s = 30.33$ µs; $L_2 = 2.65$ in. (6.7 cm); $2L_2 = 43.44$ µs; $\Delta\tau = 2L_2/V_s - 2L_1/V_s = 13.11$ µs. Measurements suggest that $\overline{\gamma}(\omega)$ is a slowly varying function of frequency as is $\overline{\alpha}(\omega)$. Thus, it is useful to examine the behavior of (6) with $\overline{\alpha}(\omega)/\overline{\gamma}(\omega) = A$, a constant. Thus:

$$\left| S_0(\omega)/2\overline{\gamma}(\omega) \right| = \cos(\pi f \Delta\tau); \qquad\qquad A = 1 \tag{7}$$

$$= 1.25 + \cos(2\pi f \Delta\tau); \quad A = .5 \tag{8}$$

Fig. 15(a) is a plot of Eq. (7) and (8), from D.C. to 400 kHz.

Because the $n = 1$ mode is cutoff in member E of Fig. 8, a periodic response similar to that of Fig. 15 does not exist.

Fig. 15(b) combines the results presented in Fig. 14 with 15(a), neglecting the $Z_1(\omega)$ in $H(\omega)$, and renormalizing the results to unity at 250 kHz.
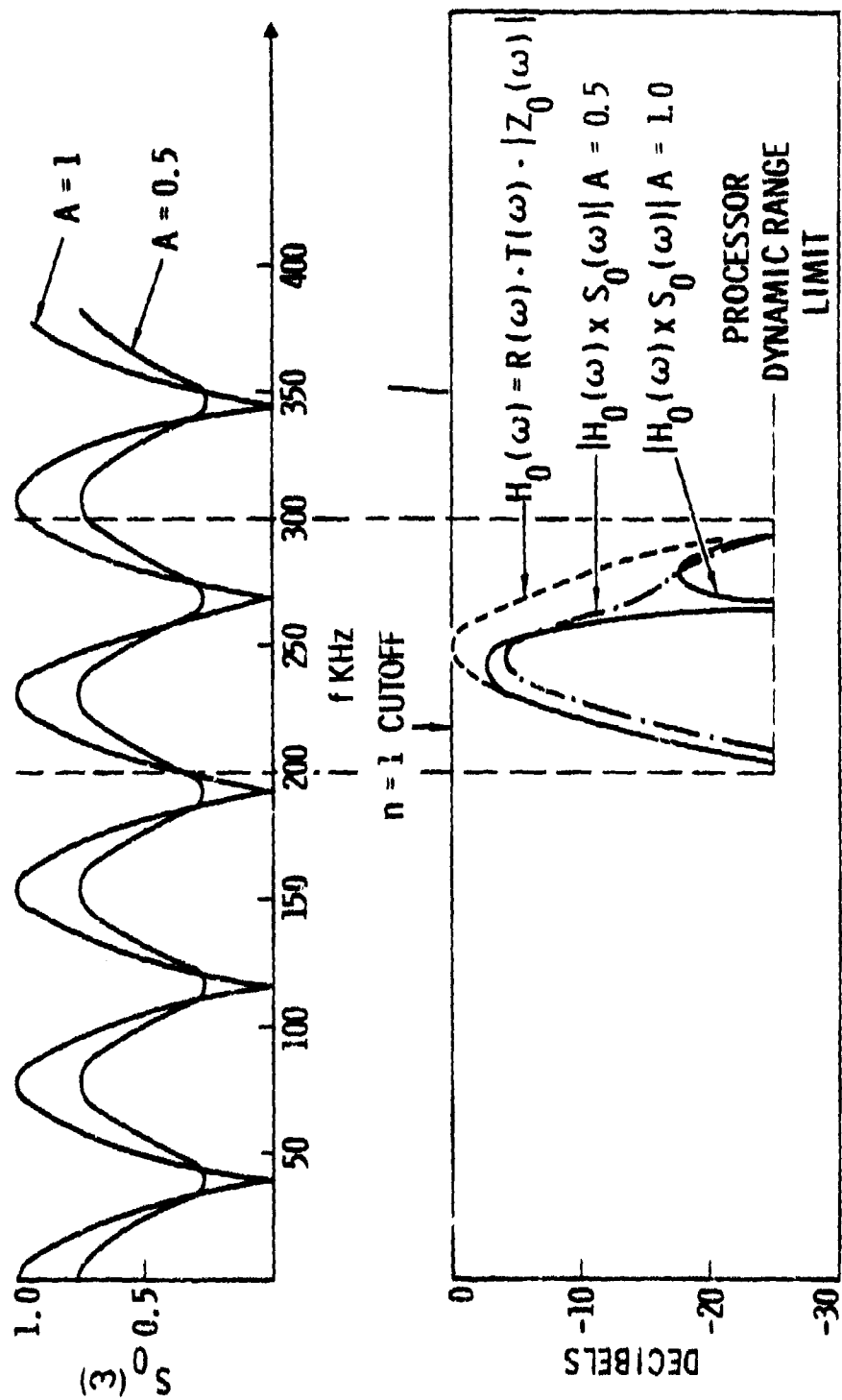
Fig. 15 Idealized Frequency Responses.

The importance of Fig. 15(a) is that, for A = 1, one would expect to observe a characteristic null in the Fourier transform of the system impulse response near 265 kHz corresponding to destructive cancellation of SH signals traveling along the two delay path illustrated in Fig. 12. If an obstruction is introduced into the L_2 path, e.g., a crack emanating from the fastener hole, then the null should be strongly affected as indicated in Fig. 15(b) for A = .5. Both theoretical predictions have in fact been observed experimentally and will be described below. Before concluding the section it should be pointed out that the structure response exhibits characteristic features that land on the skirts of our EMAT test system response where the signal to noise ratio is reduced. Improved performance could be achieved by shifting the EMAT passband down to 196 kHz. These numbers would, of course, be different for samples with dimensions different from those of the mock-up used in this work.

Early effort was directed towards using .25 in. (.64 cm) period EMATs at higher frequencies (650-850 kHz). Referring to the SH mode dispersion relation in Fig. 13, for a 9/32 in. (0.71 cm) plate t/λ = 1.125 and operation with a single higher order SH mode is possible for n = 2 or n = 3 by restricting the system bandwidth. Such an approach offered several advantages such as improved signal to noise ratio, better time resolution due to the slower velocities, and better beam collimation because of high frequency operation. The major disadvantage was that frequency of operation, excitation efficiency, and group delay were strong functions of plate thickness. Since actual wing sections do have significant geometrical variations, such added variability would further complicate data interpretation. Also the sealant in actual wing sections would affect the higher order SH modes in a more uncontrolled manner.

31

V. DESCRIPTION OF MEASUREMENT SYSTEM

A.   ELECTRONICS

A series of breadboard electronics were partially developed and
improved on the program in order to facilitate data interpretation and pattern
recognition in real time. Figure 9 gives a block diagram of the measurement
system comprising:

Function Generator - A breadboard function generator supplies digital
drive signals to the a class C power amplifier at a low pulse
repitition rate. The drive signal period, prf and pulse durations
are all adjustable. Fig. 16 shows the transmitter drive voltage,
resulting EMAT current waveforms as well as the received direct
transmission acoustic signals for two cases. There is significant
distortion present in the current because the transmitter was
designed for operation at 750 kHz and simply modified for 250 kHz
operation. In the first case, an 8-cycle, 250 kHz, tone burst is the
input, corresponding to a maximum amplitude received signal. (The
current rundown is by design to protect the transmitter from long
duration pulses, since no heat sinking is used.) The second shows
the effect of reducing the drive to two TTL pulses as is necessary in
order to minimize interference from the direct electromagnetic
feedthrough pulse. As the EMATS act as bandpass filters, the current
waveform distortion is of little practical significance. However,
the fact that a strong second, higher frequency trailing pulse
appears when the input pulse duration is reduced to two carrier
cycles clearly shows the existence of the $n = 1$ mode which propagates
slower and contains more high frequency energy than the $n = 0$ mode.

The pulse repitition rate used was 40 pps, or 25 ms/pulse, a
compromise figure. Higher rep-rates coupled with low pass filtering
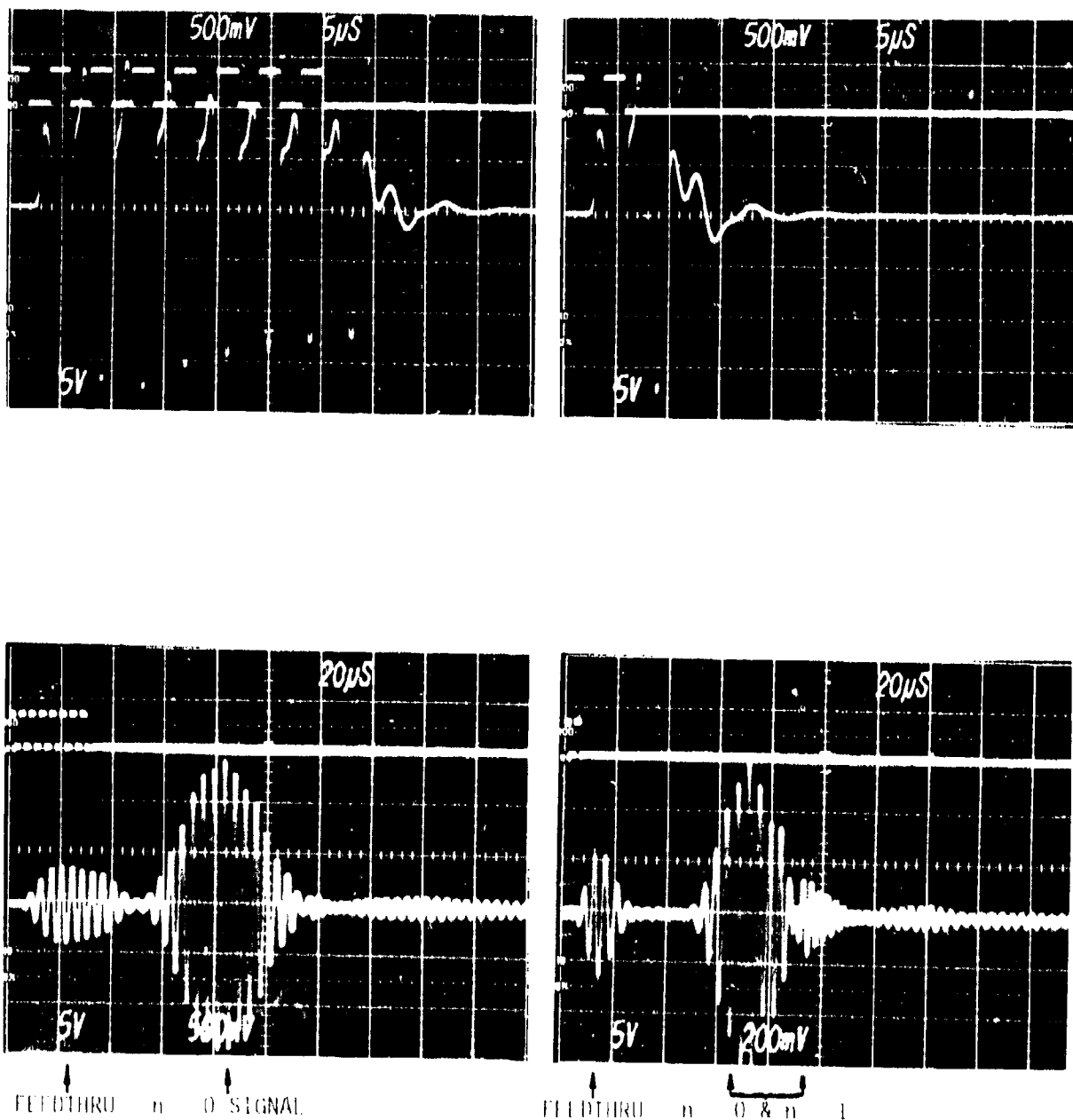
Fig. 16 Ultrasonic Waveforms.
    Top: TTL Transmitter Drive and EMAT Current Waveforms
                (5 Amp/Div) for 8 Cycle (Left) and 2 Cycle (Right)
                Excitation.
    Bottom: Received Ultrasonic Signal on a 9/32" Aluminum
                Plate. The Richer Spectral Content of the Shorter
                Pulse Excites the n = 1 Mode.

33

is advantageous for averaging out thermal noise and rapid data acquisition. However, since the acoustic Q of the aluminum mock-up was very high at 250 kHz, reverberations did not decay rapidly. Thus a high rep-rate coupled with time jitter led to significant noise like clutter interference. Fortunately, the actual wing section was long and narrow and appeared to have a significantly lower acoustic Q (possibly due to the sealant). Hence this type clutter interference was not a problem.

Receiver - The receiver shown in Fig. 9 is a four-stage discrete, fast recovery FET amplifier capable of 80 dB voltage gain. Simple single tuned stages give the response $R(\omega)$ illustrated in Fig. 14.

Correlation Processor - The analog correlation processor forms the linear product of the received acoustic signals with a known, gated reference signal in order to derive both phase and amplitude information about received acoustic signals. By using the VCO capability of the HP3312B, it is possible to sweep the frequency of the gated reference and produce a real time plot corresponding to the Fourier transform of time gate segments of the received acoustic signals. Fig. 17 gives functional block diagram of the processor board. The Ref.-1 and Ref.-2 inputs are identical TTL signals, half-bit delayed with respect to each other, and time delayed with respect to the main transmit TTL burst. The reference signals are buffered and bandpass filtered in order to suppress higher harmonics which degrade signal to noise. Thus, the ideal output of the processor may be approximated by:

$$V_x(\omega_R) = C \left\langle \int_{T_1}^{T_2} v_a(t) \cos\omega_R t \, dt \right\rangle$$
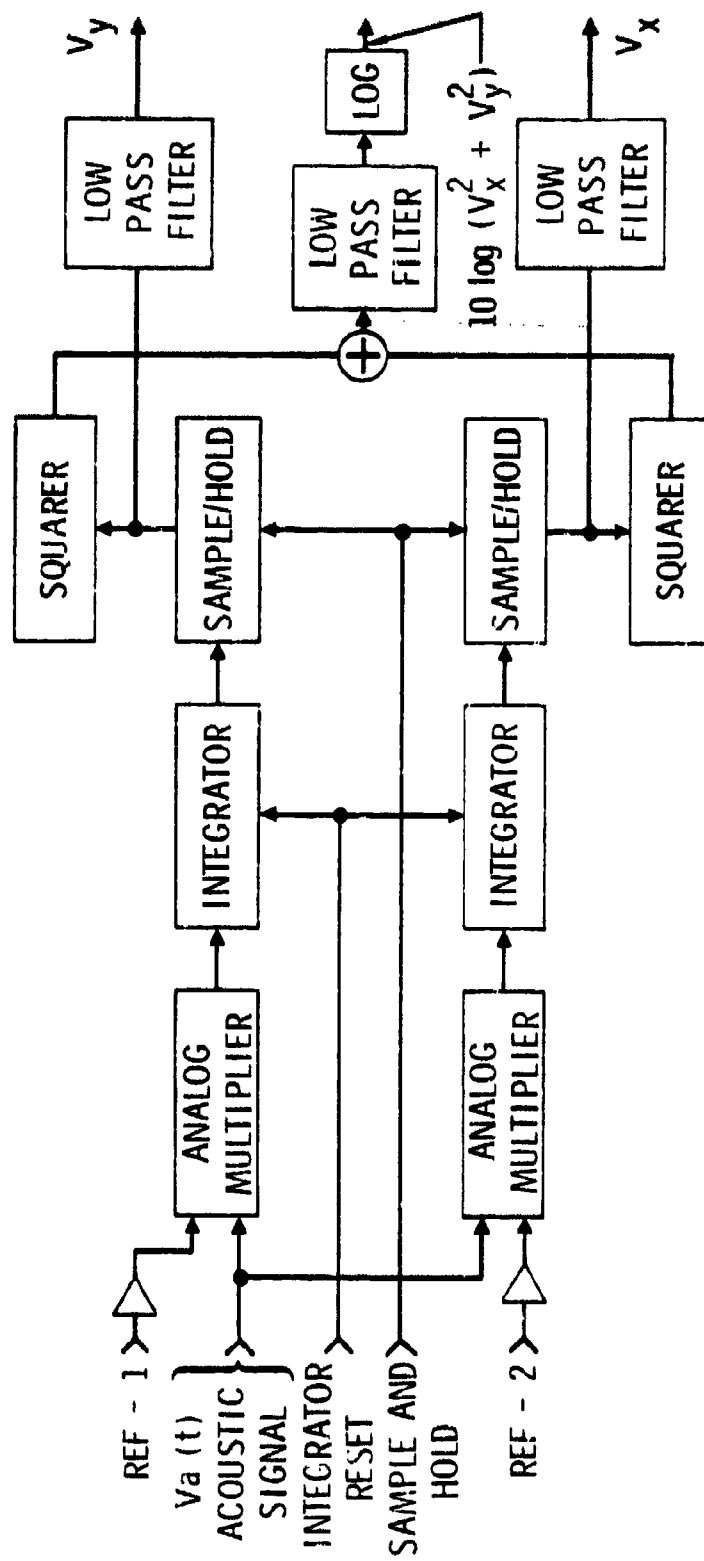
34

Fig. 17 Correlation Processor Functional Block Diagram.

$$V_y(\omega_R) = C \left\langle \int_{T_1}^{T_2} v_a(t) \sin\omega_R t \, dt \right\rangle$$

where C is a constant of proportionality and is controlled by the receiver gain adjust. The brackets denote time average. If $v_a(t)$ is a signal that vanishes outside the range $T_1 < t < T_2$ then V_x and V_y are the real and imaginary parts of Fourier transform, $f v_a(t)$, evaluated at $\omega = \omega_R$. Since the complex Fourier transform has fewer wiggles than the corresponding time waveform $v_a(t)$ in the case of overlapping time signals, it is a much simpler display to interpret. The time averaging is achieved by low pass filtering the sample and hold outputs. As a compromise between speed of data acquisition and degree of averaging we used a single, two-stage RC low pass filter and set each time constant at .033 sec. Thus, we were able to effectively average about seven sample and hold outputs at a 40 pps rep-rate (e.g., $N_{eff} = (2 \times .033 \times 40)^2$). The price paid for averaging is a slower data acquisition rate.

B.   DATA DISPLAY

Two modes of display were used. Polar plots of the locus of the complex Fourier transform were obtained by using the V_x and V_y outputs to drive an x-y recorder. Plots of the magnitude of the filter passband were obtained from the VCO voltage and log outputs. Variation of both the transducer orientation (angular dependence of scattering) and reference frequence (Fourier transform) were considered. Because of geometrical variation in the actual structure, more repeatable data was obtained from the Fourier transform approach with fixed transducer location and variable frequency.

The system dynamic range was limited to about 25 dB by error in the squaring circuit. Thermal noise was found to be below the clutter level due to acoustic reverbation in the wing section mock-up. Excellent signal to noise was observed in the actual wing section because its long and narrow shape as well as damping introduced by the sealant-filled lap joint and fasteners reduced the clutter.

Fig. 18 shows the various types of displays for a direct transmission SH signal on a 9/32 in. (0.71 cm) thick plate. The top photograph shows the received time signal in relation to the "2 cycle" TTL transmitter drive burst superimposed on one of the TTL reference signals. The power spectra (c), plotted from 200-300 kHz clearly shows the presence of the $n = 1$ mode as predicted above and illustrated in Fig. 14. Part (d) is a polar plot of the complex Fourier Transform. The fluctuation observed in (c) and (d) are not due to thermal noise, but to acoustic reverberation as discussed above.
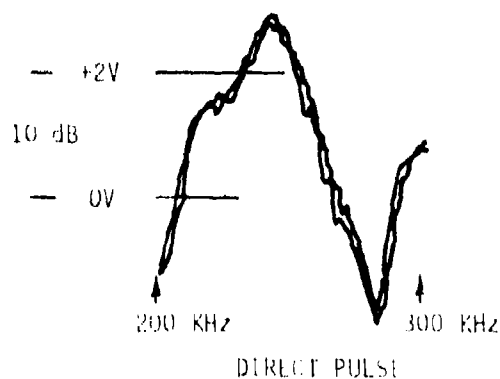
C.   EXPERIMENTAL SETUP

Fig. 19 is a sketch of the wing section mock-up we fabricated including the transducer locations. This sample was produced in our machine shop to serve as a basis for experimentation until real samples could be obtained. Fig. 20 is a photograph of the experimental setup showing the transducer fixture in position on a wing section supplied later by the Air Force. The transducers are held in fixed positions with respect to each other by the aluminum jig. The pin is used as a marker to position the apparatus properly with respect to the fastener. The breadboard custom electronics is seen toward the rear of the setup.
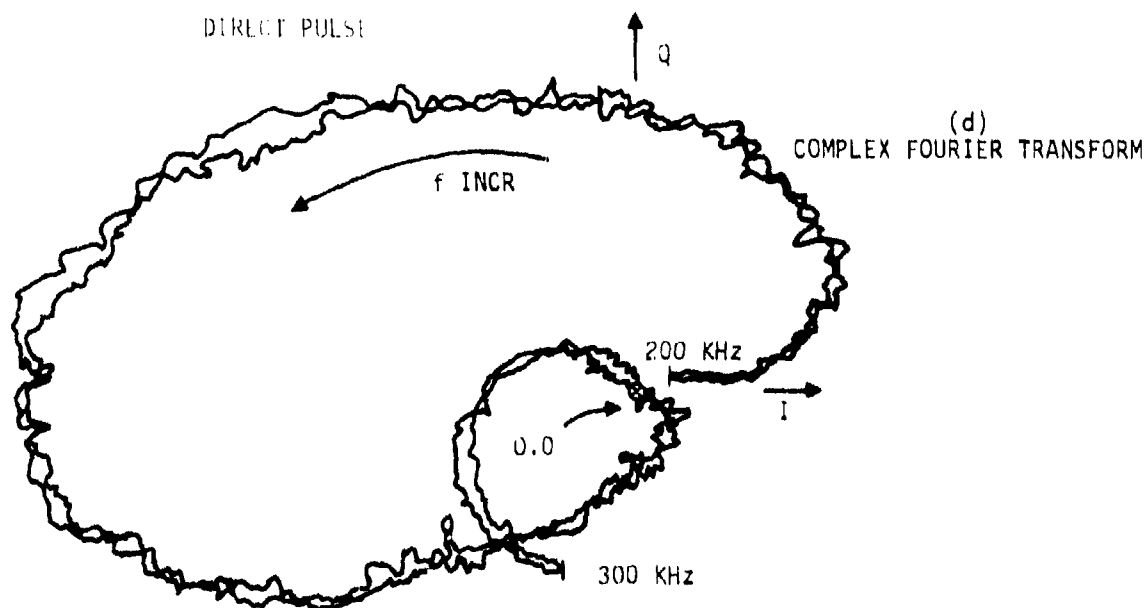
37
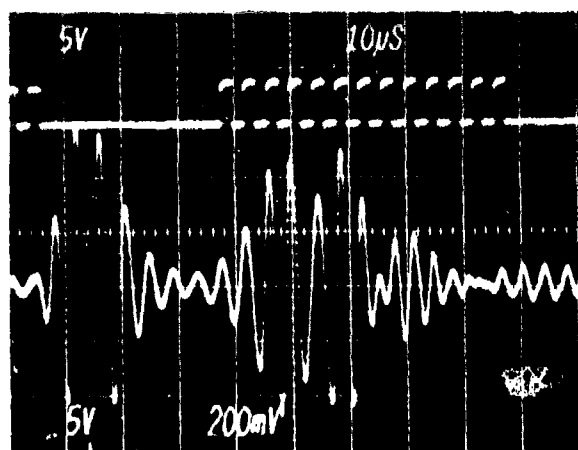
(a)
TTL DRIVE + REFERENCE

(b)
RECEIVED ULTRASONIC SIGNAL

(c)
POWER SPECTRA

(d)
COMPLEX FOURIER TRANSFORM

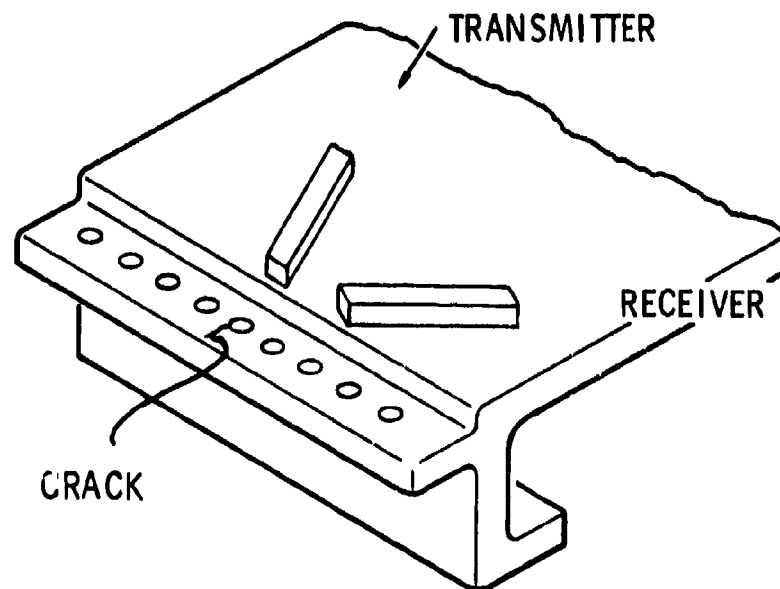Fig. 18 Time Waveforms and Real Time Fourier Transforms.
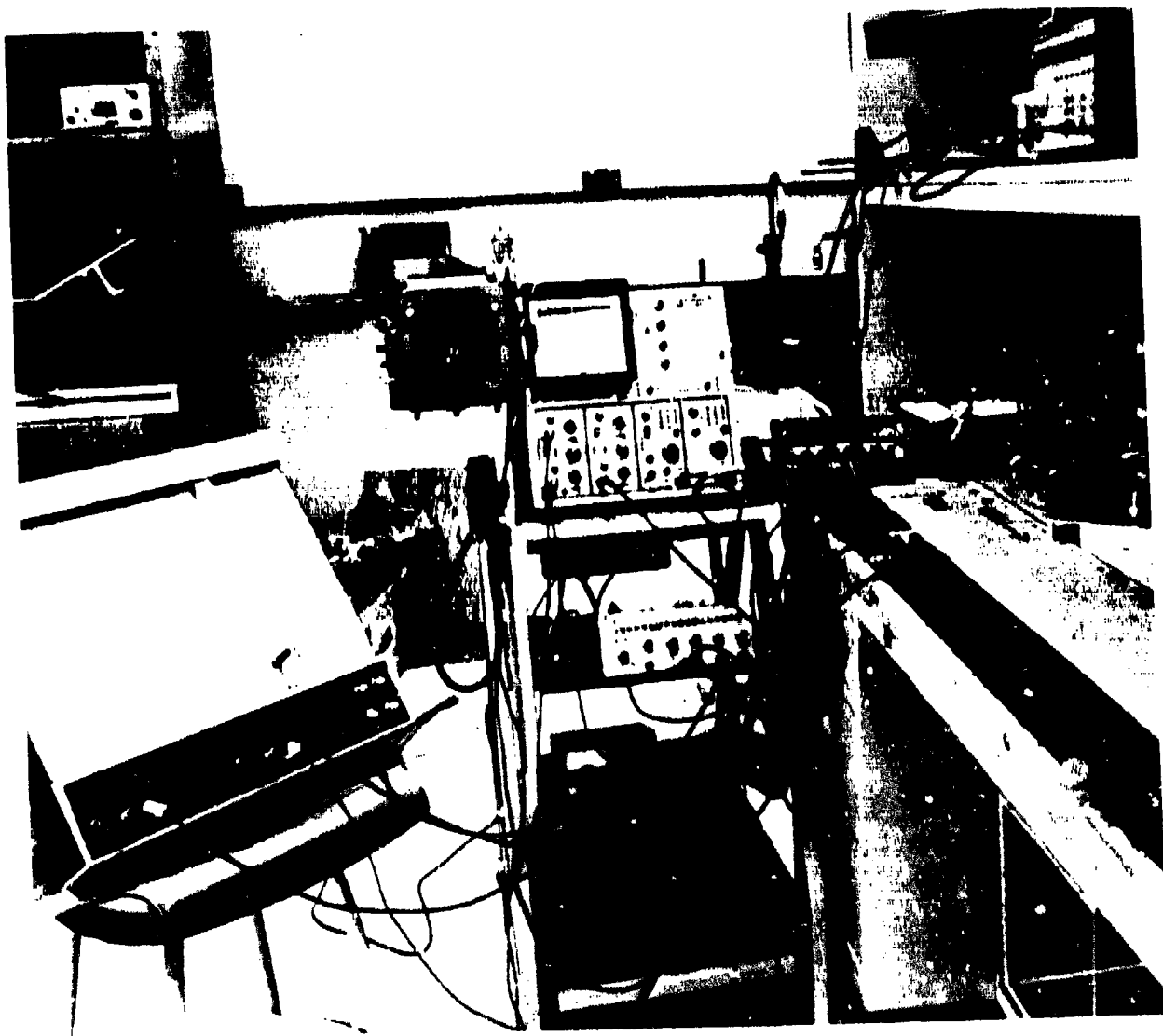
38

Fig. 19 Wing Section Mockup.

Fig. 20 Photograph of Apparatus Mounted on Wing Lap Joint.

VI. EXPERIMENTAL RESULTS

Four sets of experiments were performed. During the early part of the program, attention was directed toward the higher order modes. These measurements were made on the wing section mock-up sketched in Fig. 19. As discussed previously, their sensitivity to geometrical changes in many features of the structure made the data obtained unreliable, and hence results are not reproduced here. As a result, the fundamental mode was investigated on the mock-up, as discussed in section A below. Analysis of this data led to the theoretical model presented in section IV. Toward the end of the program, a section of a real wing became available. Section B presents the preliminary data obtained on this sample.

A.   MOCK-UP

Figs. 8 and 9 illustrated the experimental setup in which only the lower section of the lap joint was tested in the absence of fasteners and sealants. The sample was first used to optimize the electronics and establish a measurement technique that assured repeatability for an unperturbed set of holes. Then slots were placed in several holes with a jeweler's saw. The slots were cut toward the outer edge of the lower lap as was illustrated in Fig. 19.

The experimental results obtained on the mock-up are given in Fig. 21. While the time waveforms are difficult to interpret, the power spectra are not. The sharp dip appearing in the power spectrum at 270 KHz for an unslotted hole, Fig. 21(a), is in good agreement with the simple model presented above. The frequency of the dip is at the predicted location and, as the slot length is increased, the amplitude of the dip is decreased. This closely corresponds to the behavior predicted in Fig. 15. Also shown in Fig. 21 are the complex Fourier transform plots. From these it can be seen that there is phase as well as amplitude information that varies systematically with slot length. These correlations have not yet been fully

41

-0 dB

-10 dB

-20 dB

200 kHz

300 kHz

NO SLOT

0.03" SLOT

0.11" SLOT

0.20" SLOT

0.26" SLOT

(a)

V_Q

V_I

$\tilde{V}_Q$

(ω)
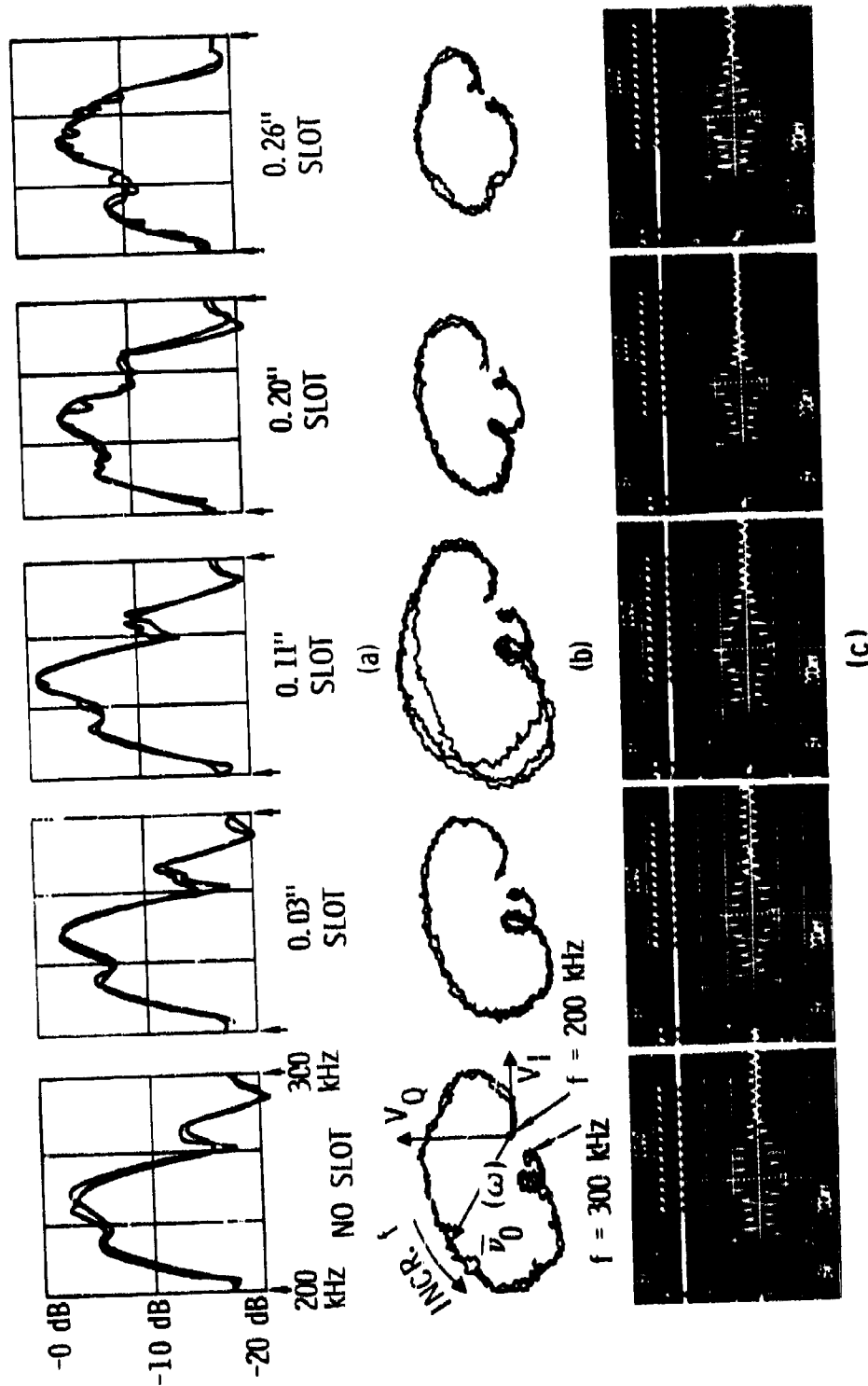
INCR

f = 300 kHz

f = 200 kHz

(b)

(c)

Fig. 21 Slot Progression on Wing Section Mockup.

pursued. Fig. 22 demonstrates the correlation between slot length and experimental results as derived from only the power spectra plotted in Fig. 21. These results were quite repeatable and encouraging. In particular, the depth of the dip at 270 kHz varies monotonically with slot length. The other features provide information about the geometry that has not yet been fully explored.

B. WING SECTION

After establishing that a reliable technique had been arrived at in a controlled experiment on a geometrically uniform wing section mock-up with no sealant or upper half of the joint, we proceeded to evaluate the technique on an actual wing section in which both the fasteners and sealant were present. No cracks were known to be present in any of the holes at the beginning of the experiment. The geometry of this wing section, shown previously in the photograph of Fig. 20, is illustrated in Fig. 23. It can be seen that there are regions in which both the width of the lap joint and the thickness of the plate vary. All holes are not shown, but those at points where the geometry changes are included.

Fig. 24 shows a set of data obtained for 34 fasteners in this wing section. The data is cleaner than that obtained onthe mock-up and presented in Fig. 21 because of the lower acoustic Q of this sample. Again a dip is observed. However, it is shifted down in frequency because of an increase in lap width with respect to that of the mock-up. The frequency of 240 kHz is again in agreement with the predictions of the model.

Inspection of Fig. 24 shows that there are considerable differences in the responses of the individual holes, and this can be related to the changes in sample geometry shown in Fig. 23. Note, however, that curves 15 through 25 exhibit extremely uniform responses because the wing section is uniform in this region. This data then demonstrates the fact that
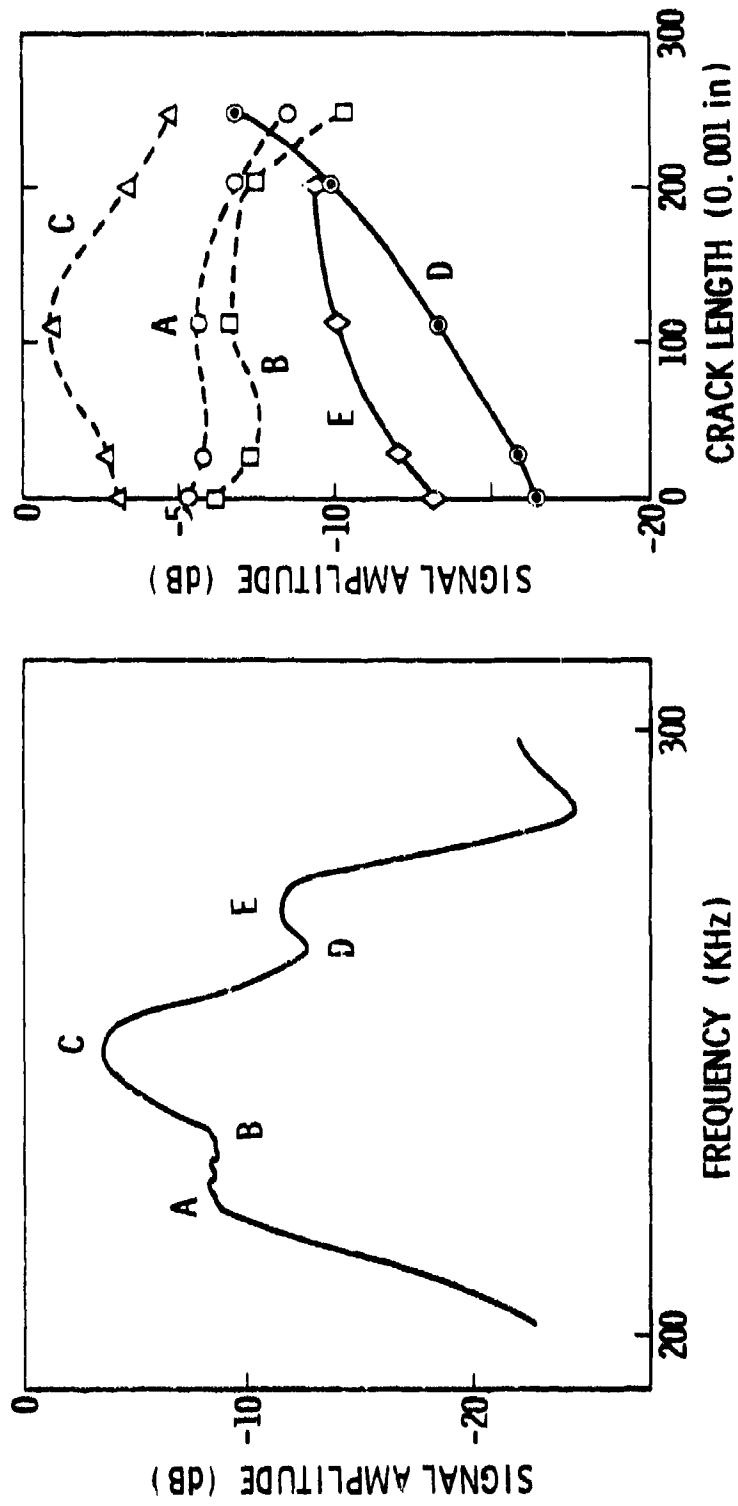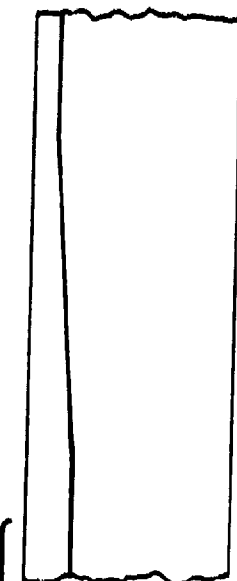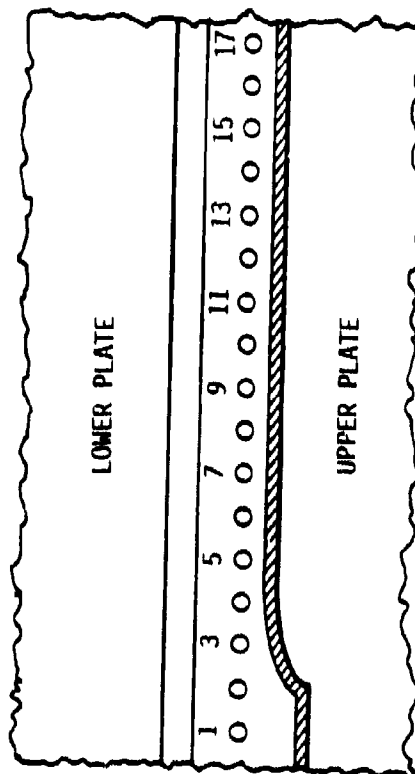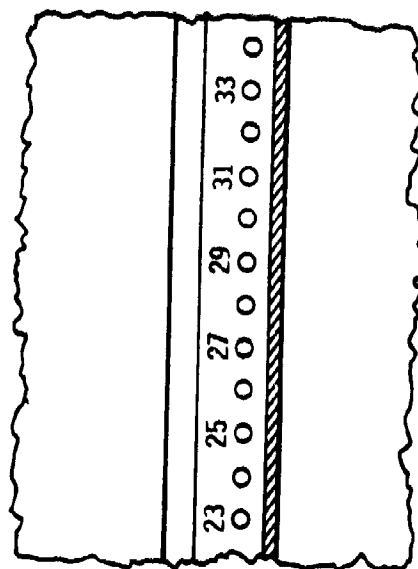
43

Fig. 22 Feature Variation with Crack Depth.

44

Fig. 23 Location of Fastener Holes with Respect to Varying Geometry of Lap Joint.
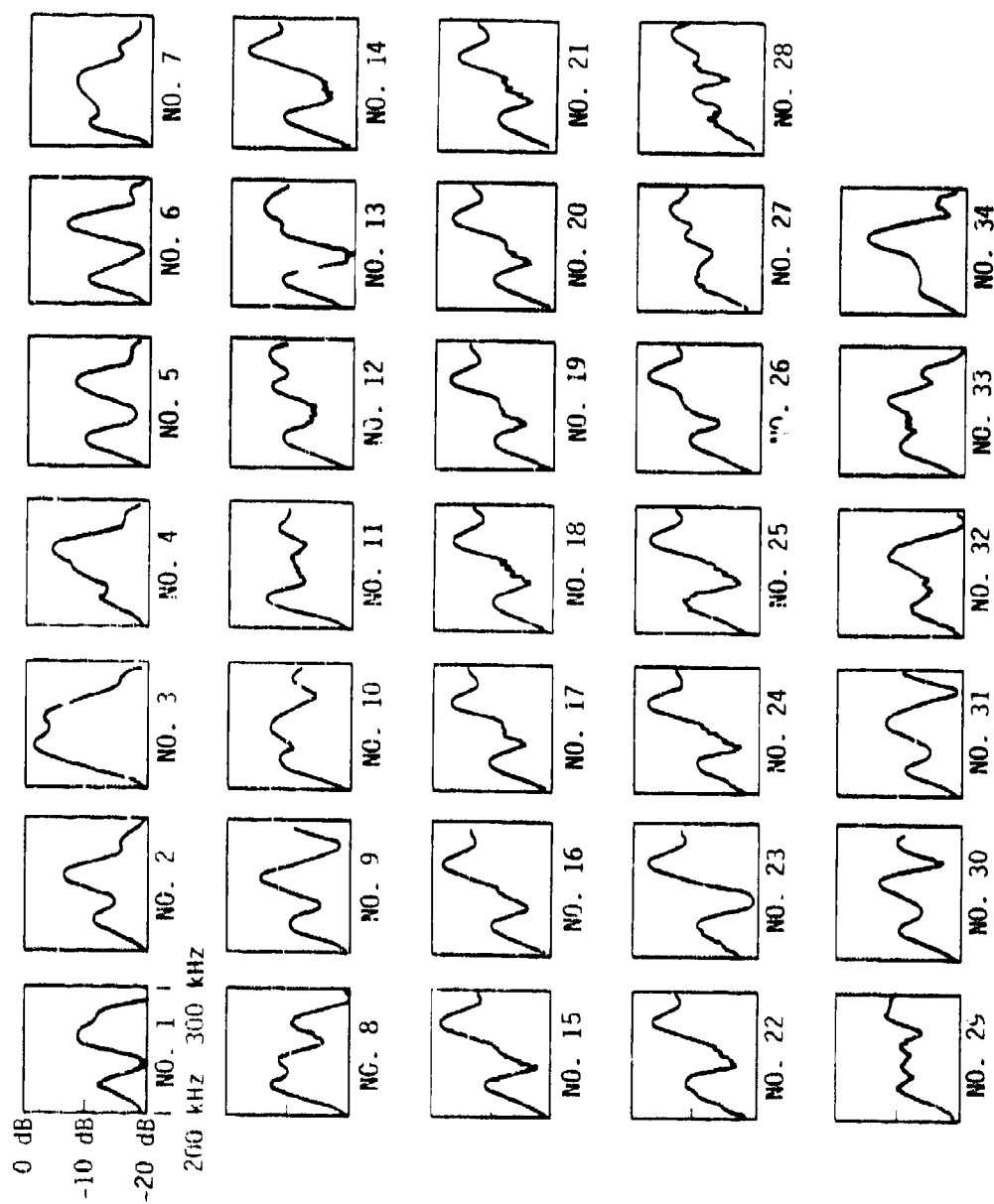
Fig. 24 Data on Wing Lap Joint.
(a) Power Spectra.

46

NO. 1 NO. 2 N NO. 4 NO. 5

NO. 6 NO. 7 NO. 8 NO. 9 NO. 10

NO. 11 NO. 12 NO. 13 NO. 14 NO. 15

NO. 16 NO. 17 NO. 18 NO. 19 NO. 20

NO. 21 NO. 22 NO. 23 NO. 24 NO. 25

NO. 26 NO. 27 NO. 28 NO. 29 NO. 30

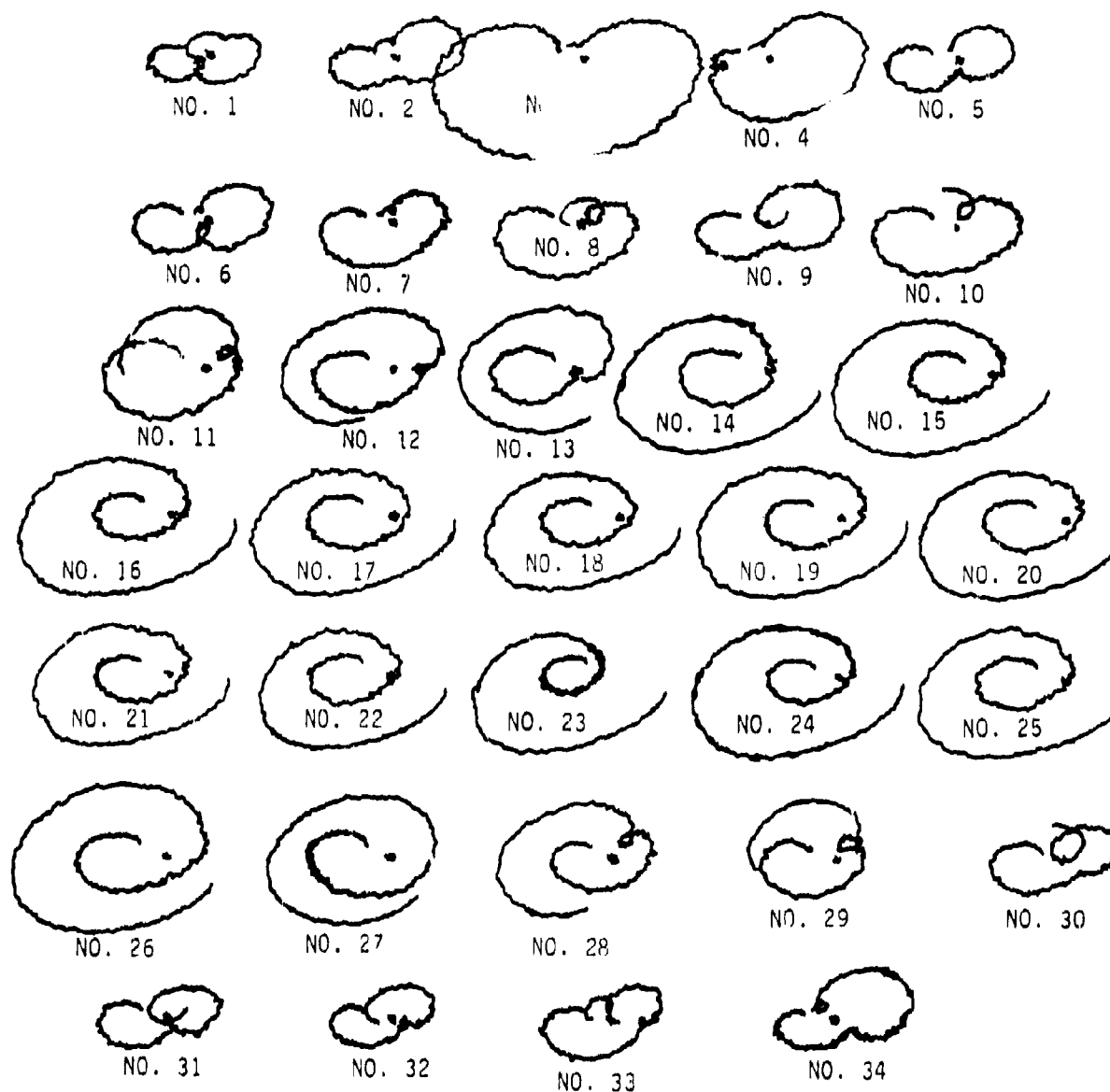NO. 31 NO. 32 NO. 33 NO. 34

Fig. 24 Data on Wing Lap Joint.
(b) Complex Fourier Transform.

47

reproducible data can be obtained on real wing sections, but that geometrical changes also influence the data.

These measurements show the background, "good fastener," response, which is somewhat different from that shown in Fig. 21 for the mock-up because the increase in width of the lap shifted the interface null down in frequency, and the presence of the sealant and upper half of the joint changes the parameters modeled by $\bar{a}$ and $\bar{\gamma}$ and thus changes the envelope of the filter passband. To test if the same procedure for detecting cracks would work in this case, we performed a controlled experiment wherein we removed a fastener and then proceeded to cut an 0.100 in. (.254 cm) slot. We were able to detect the presence of this slot, as summarized in Fig. 25. Two points are illustrated by the data. First, the presence or absence of the bolt does, in fact, change the experimentally observed spectrum. Second, under constant geometrical conditions, with bolt removed, the presence of a crack in the hole affects the spectrum in the same way as before. By comparing the last two sets of data, one sees that the depth of the null decreases as a crack appears, just as was shown for the mock-up in Fig. 22.

A final set of experiments was performed in the transmission geometry illustrated in Fig. 10. Here, measurements were made of the amplitude of the ultrasonic signal transmitted from one side of the lap joint to the other. It is initially surprising that this transmission occurs in light of previous experiments in which ultrasonic energy, injected through the top half of the lap joint, did not effectively penetrate through the sealant into the lower half. Reasons for this difference are discussed in Appendix A.

Fig. 26 shows a waveform photo and the power spectra data for the geometry of Fig. 10 in which the transmission through the joint was monitored. Thus the wave was launched by the upper left transducer in Fig. 10, and was detected by the lower right transducer after passing through the joint.
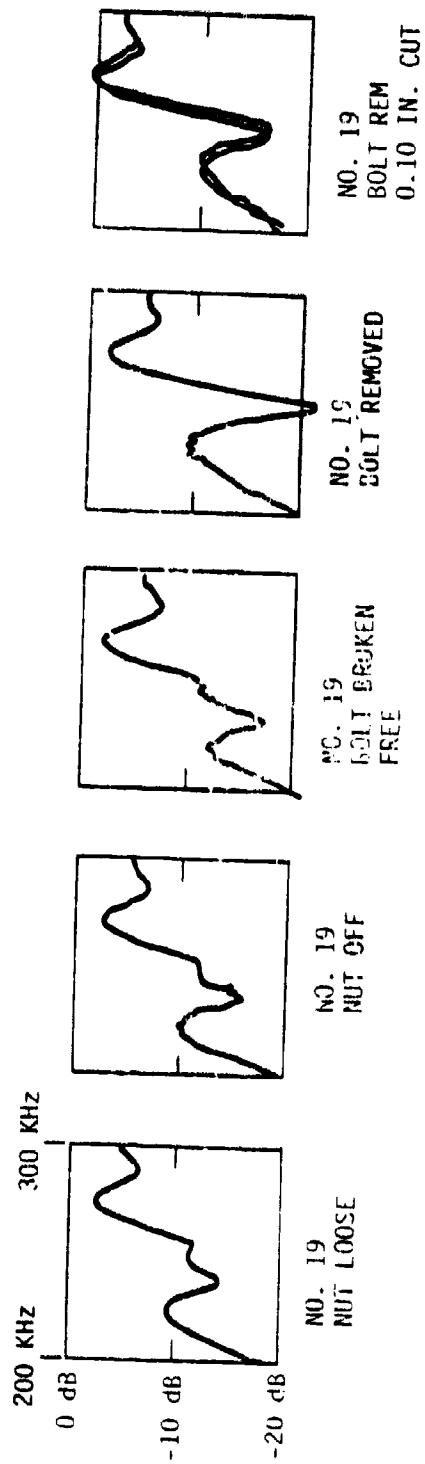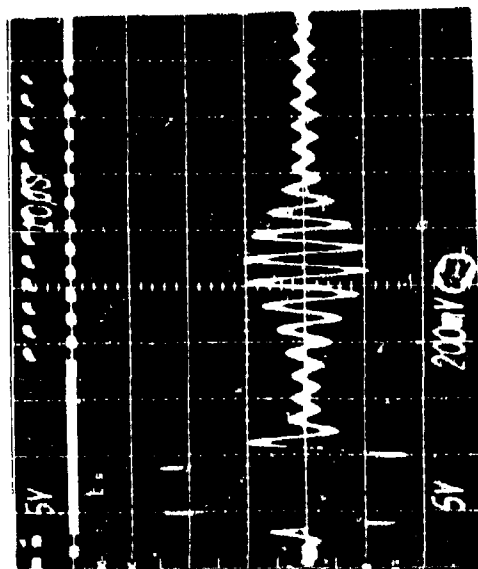
Fig. 25 Fastener and Slot Effects on Wing Sample.
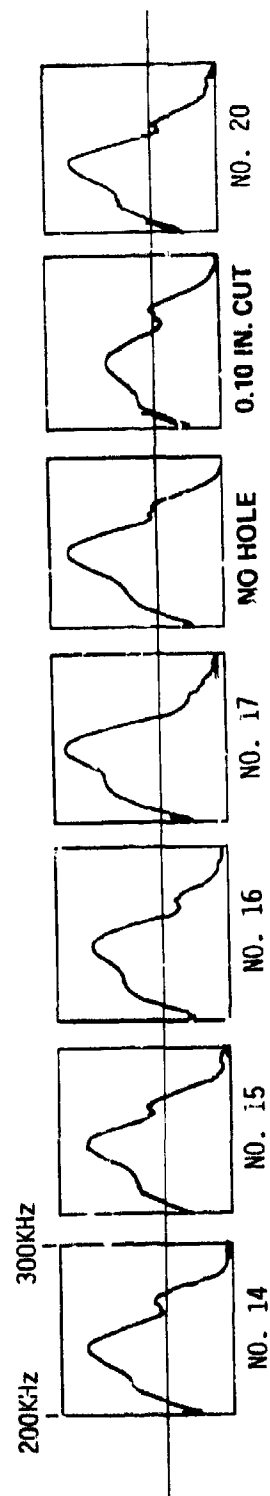
49

TRANSMISSION
FASTENER NO. 20

Fig. 26 Transmission Power Spectra.

NO. 14   NO. 15   NO. 16   NO. 17   NO HOLE   0.10 IN. CUT   NO. 20

200KHz   300KHz

50

A rather dramatic change in the energy transmitted past the previously slotted hole No. 19 and into the other half of the lap joint is observed, even after the fastener had been reinstalled. It appears likely that the presence of the crack substantially interrupts the transmission of energy across the interface and thereby is being accurately detected, a quite exciting result. However, further experiments are needed to be certain that the result was not caused by damage to the sealant during the removal and reinsertion of the fastener.

VII. CONCLUSIONS AND RECOMMENDATIONS

In this five-month feasibility study we have demonstrated that:
(1) EMATS placed on the outer wing surface can be used to excite ultrasonic energy which can propagate to and return from the fastener region of the lower section of a wing lap joint, (2) information relating to the fastener hole integrity is contained in both signals reflected from the joint and transmitted through the joint to the other plates, and (3) real time Fourier analysis is useful in deducing flaw information from the complex ultrasonic response. For the case of a lap-joint of controlled geometry and without sealant or fastener present, it has been established that: (4) saw slots as small as 0.030 in. can be detected and (5) an acoustic model has been developed which explains many features of the experimental data and aids in its interpretation and in system optimization. A limited numer of experiments has been performed on complete lap joints. Encouraging results have been obtained, including: (6) the detection of a 0.100 in (.254 cm) slot and (7) the establishment that the instrumental response is reproducible in regions of constant geometry. However, further work is required to separate the flaw information from that introduced by variations in overlap of the plates, by the fastener, and by coupling to the other plate through the sealant in regions where these geometrical features are not constant.

Future efforts will require: (1) optimization of system design to improve the precision of the data (2) development of more sophisticated data gathering, processing, and interpretation procedures to separate the flaw information from the unwanted background, and (3) a more extensive, low frequency experimental verification to establish a statistically significant foundation for field application of this technique. A more detailed plan will be submitted under a separate cover.

52

APPENDIX A -- EFFECTS OF SEALANT

Fig. A-1 illustrates two cases of practical interest in inspecting lap joints: (1) that of a shear or longitudinal wave normally incident upon an aluminum-polyethelene-aluminum interface and (2) that of an n = 0, SH mode propagating along an infinite aluminum-polyethelene-aluminum sandwich structure. Polyethelene is used to simulate the acoustic effects of a sealant, whose properties we have not characterized. Case (1) relates to the situation which occurs during inspection through the upper sheet with a device like the Rotoscanner. Case (2) occurs during inspection of the type discussed in this report.

Normal Incidence

The respective shear and longitudinal wave velocities, in units of km/sec, for aluminum (density ρ_a = 2690 kg/m^3) and polyethelene (ρ_p = 886 kg/m^3) are: V_s = 3040, 540; V_L = 6420, 1950. The relative acoustic impedances of the two materials are Z_p/Z_a = .0585 and .1011 for shear and longitudinal waves, respectively. We measured the thickness of the sealant to be about 5 mils in our sample. It possibly varies from 1-10 mils throughout the structure. Taking a 5 mil nominal thickness we find that the adhesive thickness is $\lambda/4$ at 1.06 MHz for a normally incident shear wave and at 3.84 MHz for a longitudinal wave. Thus it follows from simple transmission line analysis that strong reflection loss peaks will occur at the quarter wave frequencies given by (2 m + 1) x 1.06 MHz and (2 m + 1) x 3.84 MHz for shear and longitudinal waves, respectively. Thus, for a double pass, a loss due to reflection of 36 dB for shear waves and 28 dB for longitudinal waves is to be expected at their respective quarter wave frequencies.

At first glance one would expect transmission bands to occur at the half wave frequencies, but as indicated in Fig. A-2, they are quite narrow. Furthermore, a variation in sealant thickness of from 5.7-8.8 mil would shift
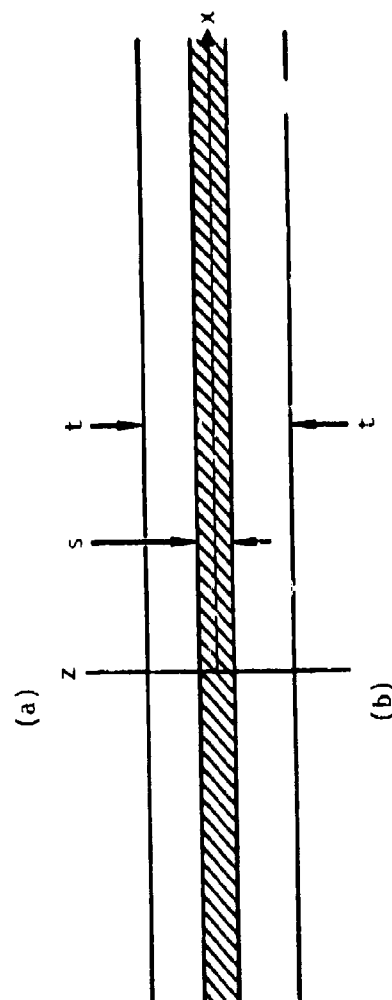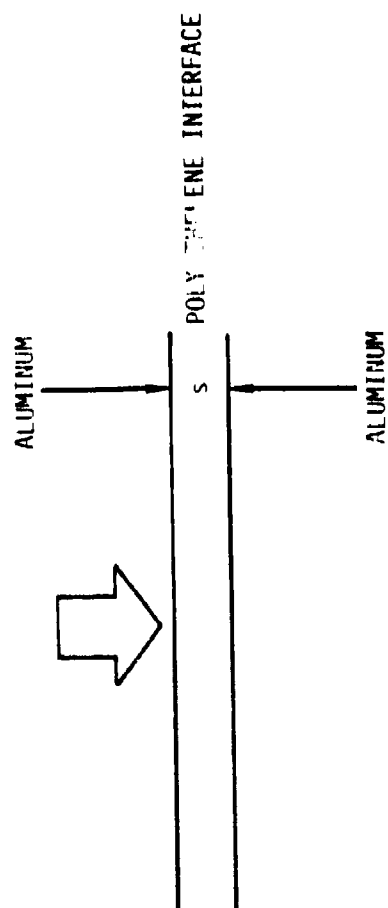
53

Fig. A-1 Two Important Geometries Displaying the Effect of Sealant (Modeled by Polyethelene) on Ultrasonic Propagation.
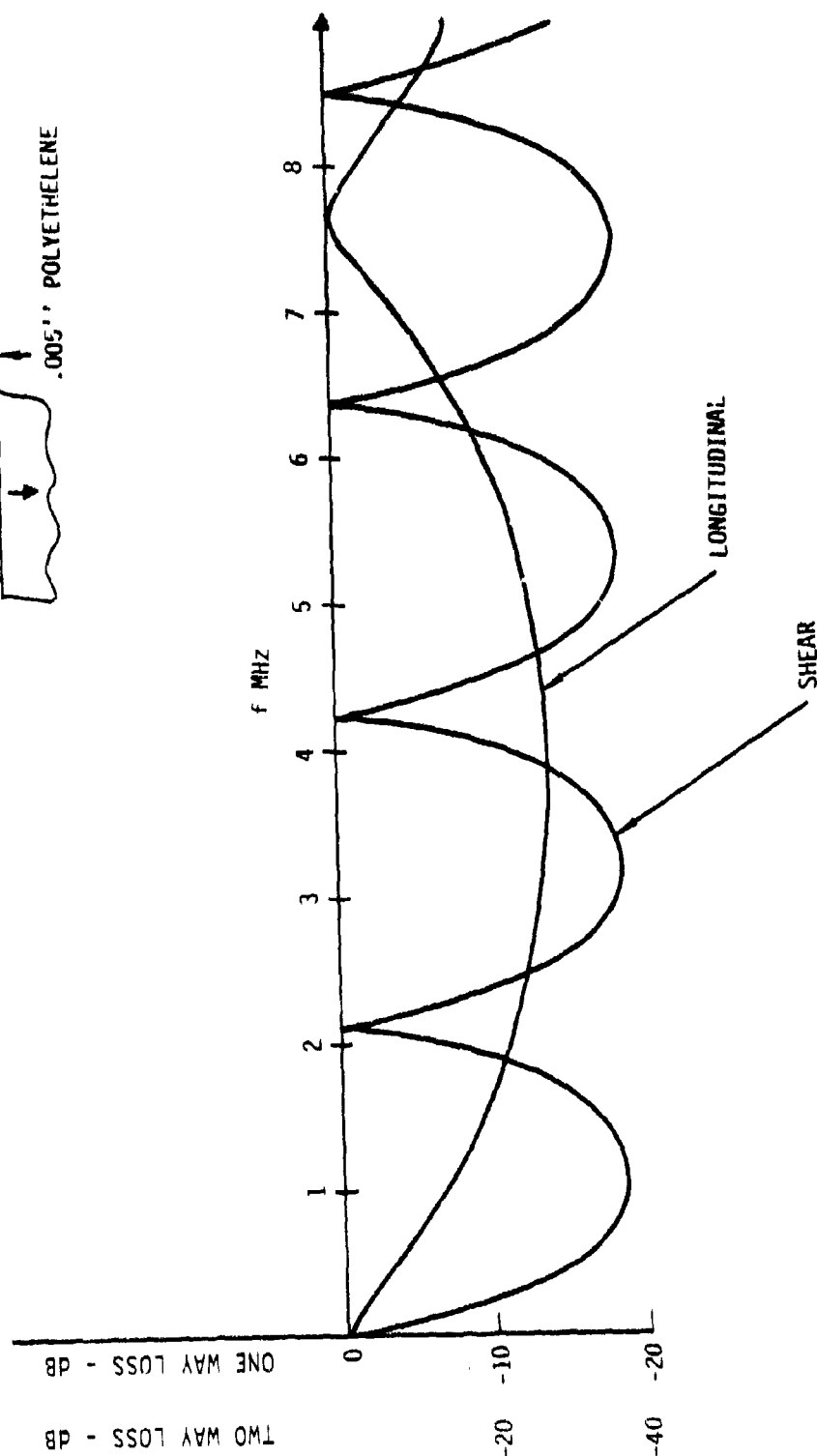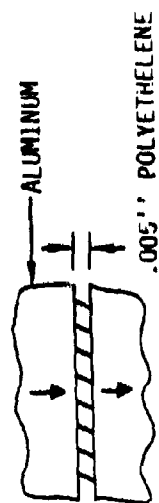
Fig. A-2 Normal Incidence Transmission Through 0.005" Thick Polyethelene Layer.

55

the quarter wave frequency of a shear wave transmission over the 3-6 MHz band. One would then expect severe phase distortion of a pulse and strong variation from point to point on the sample. Similar effects are expected for longitudinal wave transmission. Hence, it is not practical to inspect ultrasonically the lower lap joint from the top surface with a small, high-frequency piezoelectric transducer probe.

Plate Modes

Experiments with low order SH waves in sandwich structures of the type in Fig. A-1(b) indicate that, at a frequency of 250 kHz, the $n = 0$ mode is only slightly perturbed by the sealant. At this frequency, the thin, slow layer can transmit a shear stress easily from the top plate to the bottom plate. Thus good, $n = 0$, SH wave transmission is to be expected through the lap joint with reflection introduced by the step discontinuities. However, sealant variations may introduce uncontrolled amplitude variations in the transmission through and reflection from a lap joint if the frequency is not sufficiently low enough to cut off all higher order modes that can be supported by an aluminum-sealant-aluminum sandwich structure.

Since the analysis of the structure of Fig. A-1(b) is quite straightforward for SH waves, it will be presented here. For no y-variation and x-propagation, we require the stress component T_4 vanish at $z = \pm t/2$. Also, T_4 and the particle velocity V_y are continuous at $z = \pm s/2$. The boundary conditions are separable, hence each mode satisfies the above boundary conditions individually:

Region 1

$$V_y = A_n \cos k_{zn} (z - t/2) \tag{1}$$

$$T_4 = - \frac{\rho V_s^2}{j\omega} A_n k_{zn} \sin k_{zn} (z - t/2) \tag{2}$$

56

Region 2

$$V_y = B_n \cos k'_{zn} z \qquad \qquad (3)$$

Symmetric

$$T_4 = - \frac{\rho' V'_s{}^2}{j\omega} k'_{zn} \sin k'_{zn} z \qquad (4)$$

$$V_y = B_n \sin k'_{zn} z \qquad \qquad (5)$$

antisymmetric

$$T_4 = + \frac{\rho' V'_s{}^2}{j\omega} k'_{zn} \cos k'_{zn} z \qquad (6)$$

Region 3

$$V_y = C_n \cos k_{zn} (z + t/2) \qquad (7)$$

$$T_4 = - \frac{\rho V_s{}^2}{j\omega} C_n k_{zn} \sin k_{zn} (z - t/2) \qquad (8)$$

and

$$k_x = \sqrt{k_s{}^2 - k_z{}^2} = \sqrt{k'_s{}^2 - k'_z{}^2} \qquad (9)$$

Because the structure is symmetrical, the analysis is straightforward. By taking the ratio T_4/V_y z = + s/2 one obtains the dispersion relation relating k_x to ω. Once this relation is known, then B_n and C_n are given simply in terms of A_n from continuity of V_y at z = ±s/2 and the source free problem is solved.

57

Dispersion Relations

Symmetric Case

$$k_{zn} \tan k_{zn} (s/2 - t/2) = \frac{\rho'V'^2_s}{\rho V^2_s} k'_{zn} \tan k'_{zn} s/2 \qquad (10)$$

Antisymmetric Case

$$k_{zn} \tan k_{zn} (s/2 - t/2) = - \frac{\rho'V'^2_s}{\rho V^2_s} k'_{zn} \cot k'_{zn} s/2 \qquad (11)$$

Cutoff Frequencies

Denoting the symmetric and antisymmetric cutoff frequencies corresponding to $K_x = 0$, by f_{sn} and f_{an}, respectively, one finds that the dispersion relation at cutoff reduces to:

Symmetric

$$\tan \left[\pi \frac{f_{sn}}{V_x} t(1 - s/t) \right] = - \frac{\rho'V_s'}{\rho V_s} \tan \left(\pi \frac{f_{sn}S}{V_s'} \right) \qquad (12)$$

$$= - .0585 \tan \left(\pi \frac{f_{sn}S}{V_s'} \right) \qquad (13)$$

Antisymmetric

$$\tan\left[\pi \frac{f_{an}t}{V_s}(1 - s/t)\right] = + \frac{\rho'V_s'}{\rho V_s}\cot\left(\pi \frac{f_{an}S}{V_s'}\right) \tag{14}$$

$$= + .0585\cot\left(\pi \frac{f_{an}S}{V_s'}\right) \tag{15}$$

The limiting case of S = 0 yields

$$f_{sn} = \frac{nV_s}{t} \tag{16}$$

$$f_{an} = \frac{(2n + 1) V_s}{2t} \tag{17}$$

n = 0, 1, 2, 3, etc.

which corresponds to the cutoff frequencies of a solid aluminum plate of thickness t. As S is increased from 0, but remains small compared to t, the cutoff frequencies are shifted. Analysis shows that the phase velocity of the lowest order symmetric SH mode, which has no cutoff frequency, is perturbed less than 0.65% for t = 250 and S < 10 mils. This mode is the analog of the n = 0 mode for a single plate. If we restrict our frequency of operation below the cutoff frequency for the next mode, f_{ao}, corresponding to the n = 1 mode of a simple plate, the effects of sealant variations will be negligable. Unfortunately, from (15), one finds the presence of a soft material such as polyethelene or sealant drops the cutoff frequency to the 100-150 KHz regime for S on the order of 2-5 mil and down to the 50-100 KHz regime for S ~ 10 mil. We know EMATS can be designed in the range but we must determine if resolution becomes a limiting factor if in fact one needs to operate at such low frequencies. A more complete characterization of the sealant coupled with the above analysis is required.